International Journal of Engineering Science 191 (2023) 103881

Contents lists available at ScienceDirect

International Journal of Engineering Science

journal homepage: www.elsevier.com/locate/ijengsci

Programming and physical realization of extreme three-dimensional responses of metastructures under large deformations☆

Weichen Li [a], Yingqi Jia [a], Fengwen Wang [b], Ole Sigmund [b], Xiaojia Shelly Zhang [a,c,d,*]

[a] Department of Civil and Environmental Engineering, University of Illinois Urbana-Champaign, 205 North Mathews Ave, Urbana, IL 61801, USA
[b] Department of Civil and Mechanical Engineering, Technical University of Denmark, Koppels Allé, Building 404, 2800 Kongens Lyngby, Denmark
[c] Department of Mechanical Science and Engineering, University of Illinois Urbana-Champaign, 1206 W. Green St., Urbana, IL 61801, USA
[d] National Center for Supercomputing Applications, University of Illinois Urbana-Champaign, USA

ARTICLE INFO

Keywords:
3D programmable mechanical response
Inverse design
Physical realization
Experimental validation
Multi-phase and heterogeneous mechanisms
Multimaterial topology optimization

ABSTRACT

Structures and materials with programmable mechanical responses are desirable for many applications. Great advancement has been achieved and led to the discovery of metastructures/metamaterials with unconventional programmed properties. While most established studies focus on two-dimensional (2D) or pseudo-three-dimensional systems, certain complex deformations and functionalities can only be realized in three-dimensional (3D) space. The lack of comprehensive exploration of programmable large-deformation kinematics in 3D space could leave out a plethora of 3D deformation mechanisms, structural geometries, and complex responses that may lead to unprecedented mechanical functionalities. Based on multimaterial inverse design by topology optimization, this study systematically investigates several precisely programmed nonlinear extreme responses in 3D structures under finite deformations. Sophisticated 3D geometries with unique deformation capabilities are discovered. Under monotonic loading, extreme behaviors such as self-recovering counter-rotation and sequential lateral expansion–contraction are created, which are beyond the reach of 2D structures. The associated mechanisms fully exploit 3D space and optimally harness free-form geometries, material nonlinearity, the large disparity in material properties, and large rotations to deliver the target responses. Some discovered mechanisms are heterogeneous in space and asynchronous in time, spatially consisting of a series of sub-mechanisms. Albeit with complex geometries, the optimized structure with multi-phase and heterogeneous mechanisms is accurately fabricated through a proposed hybrid fabrication method tailored for 3D geometries combining 3D printing and casting, and the design's unique programmed behavior is validated. The experimentally measured response shows high agreement with the prescribed target and numerically programmed responses. The discovered unique 3D deformation patterns and designs, underlying mechanisms, tailored 3D fabrication approach, and experimental procedures

---

☆ Authors X.S.Z., W.L., and Y.J. acknowledge the support from U.S. National Science Foundation (NSF) CAREER Award CMMI-2047692 and U.S. NSF EAGER grant CMMI-2127134. Authors O.S. and F.W. acknowledge the support from the Villum Foundation Villum Investigator Project “InnoTop”, Denmark.

The funding sources had no involvement in the study design; in the collection, analysis, and interpretation of data; in the writing of the manuscript; and in the decision to submit the article for publication.

* Corresponding author at: Department of Civil and Environmental Engineering, University of Illinois Urbana-Champaign, 205 North Mathews Ave, Urbana, IL 61801, USA.

E-mail address: zhangxs@illinois.edu (X.S. Zhang).

https://doi.org/10.1016/j.ijengsci.2023.103881
Received 8 July 2022; Received in revised form 29 April 2023; Accepted 29 April 2023

Available online 12 June 2023
0020-7225/© 2023 Elsevier Ltd. All rights reserved.

could provide meaningful mechanics insights and guidelines for realizing function-oriented mechanical metastructures/metamaterials that fully harness 3D space.

1. Introduction

Precise realization of novel nonlinear mechanical responses (deformation patterns and force–displacement relations) benefits many applications such as energy absorbers (Frenzel, Findeisen, Kadic, Gumbsch, & Wegener, 2016; Fu, Zhao, & Jin, 2019) and flexible electronics (Chen et al., 2018; Xue, Song, Rogers, Zhang, & Huang, 2020). Through the design of structural/material geometry, a wide range of unconventional and tunable responses can be realized, including auxetic behaviors (Wang, 2018; Wang, Sigmund and Jensen, 2014), tunable elastic material properties (Sigmund, 1994, 1995), elastic wave cloaking (Chen, Nassar, & Huang, 2021), and tunable buckling (Jiao & Alavi, 2018; Restrepo, Mankame, & Zavattieri, 2015; Zhang, Velay-Lizancos, Restrepo, Mankame, & Zavattieri, 2021) and wrinkling behaviors (Li, Zhu, Qi, Kang and Luo, 2021; Yang, Fu, & Xu, 2020). This study focuses on the systematic discovery of three-dimensional (3D) multimaterial structures with unprecedented mechanical behaviors under large deformations.

Among various design approaches, topology optimization (Bendsøe & Kikuchi, 1988; Bendsøe & Sigmund, 2003; Wang, Zhao, Zhou, Sigmund, & Zhang, 2021) has been very efficient in the inverse design of unique materials and structural properties. At the material level, topology optimization is used to generate metamaterials with negative Poisson's ratios (Wang, 2018; Wang, Sigmund et al., 2014), tunable elastic modulus (Sigmund, 1994, 1995), target stiffness and strength (Wang & Sigmund, 2021), programmable stress–strain relations (Wang, 2018; Wang, Lazarov, Sigmund and Jensen, 2014), and lattice structures with spatially variant homogenized properties (Zhang, Wang, & Kang, 2019). At the structural level, topology optimization is adopted to design slender structures with controlled snap-through (Bruns & Sigmund, 2004) and hardening/softening (da Silva, Beck, & Sigmund, 2020; Lee, Detroux, & Kerschen, 2020) responses. More recently, topology optimization with multiple nonlinear materials is employed to design planar composite structures with a wide variety of force–displacement ($F-D$) responses under large deformations (Li, Wang, Sigmund and Zhang, 2021). The inclusion of multiple dissimilar materials significantly expands the design space and yields behaviors unattainable by a single material. Although highly complex, two-dimensional (2D) multimaterial optimized designs have been effectively fabricated using different elastomers, and a wide range of in-plane (i.e., 2D) programmed behaviors are accurately realized and validated by experiments (Li, Wang, Sigmund, & Zhang, 2022).

Mechanical response programming has been carried out mainly for 2D and pseudo-3D structures containing single materials while being mostly absent for general 3D multimaterial structures with highly coupled finite deformations in three dimensions. Yet, many useful (and complex) responses are driven by 3D coupled deformations and are physically unavailable in 2D space. The lack of design strategy for the discovery of arbitrarily prescribed 3D deformation patterns may result in an insufficient systematic understanding of unconventional 3D responses, which could leave aside many valuable yet unexplored 3D structural mechanisms.

Free-form programming of 3D nonlinear mechanical responses into composite structures encounters several challenges. First, the associated nonlinear state equations can be challenging to handle because of the global and local structural instability, in which multiple solutions can exist and advanced numerical techniques are required. Second, the associated computational cost of solving the 3D nonlinear state equations involving finite deformations with multiple material constituents and obtaining corresponding design gradients is highly challenging, which calls for parallel computing, scalable codes, and advanced solvers. Third, the inverse design problem is highly nonconvex and may possess many local minima, leading to parameter-dependent optimization results.

Based on topology optimization, this study explores 3D kinematics space and harnesses multiple hyperelastic materials with dissimilar properties to accurately program both extreme 3D deformation patterns and force–displacement ($F-D$) relations into 3D composite metastructures. As shown in Fig. 1, with unconventional geometries and nonuniform heterogeneous material distributions, the optimized 3D multimaterial structures exploit a wide variety of non-monotonic and non-uniform mechanisms with highly coupled 3D deformations to precisely produce diverse target deformation patterns. Under continuous monotonic loading, these unique 3D behaviors include self-recovering horizontal rotation-then-counter-rotation and sequential lateral expansion-then-contraction, which are beyond the reach of 2D structures. The discovered 3D mechanisms exhibit features fundamentally different from established ones, as they consist of multiple sub-mechanisms in 3D space and develop phase changes between disparate sub-mechanisms during monotonic loading. Albeit complex in geometry, one optimized design is fabricated with elastomer and tested (Fig. 1D). Experimental result shows high agreement with the simulation results and prescribed target, demonstrating physical and precise realization of the unconventional programmed responses. The complete procedure of inverse design, hybrid fabrication, and validation is described in Supplementary Video S1. The optimized structures, unconventional 3D deformation patterns, and underlying mechanisms could provide new insights and guidelines for the design of advanced function-oriented metastructures.

The remainder of the paper is organized as follows. Section 2 briefly introduces finite elastostatics and the mathematical formulation of the inverse design problem. Section 3 presents the mathematical formulation of inverse design for mechanical response programming. Sections 4 and 5 study two families of optimized multimaterial structures programmed with unique target responses and elucidate the underlying mechanisms. The proposed hybrid fabrication method and experimental validation are included in Section 6. Concluding remarks are provided in Section 7. Four Appendices elaborate design parameterization, energy interpolation scheme, fabrication and characterization of PDMS, and experimental setup. Four Supplementary Videos provide additional details on inverse design process, deformation mechanisms, and experimental validation for the metastructures.

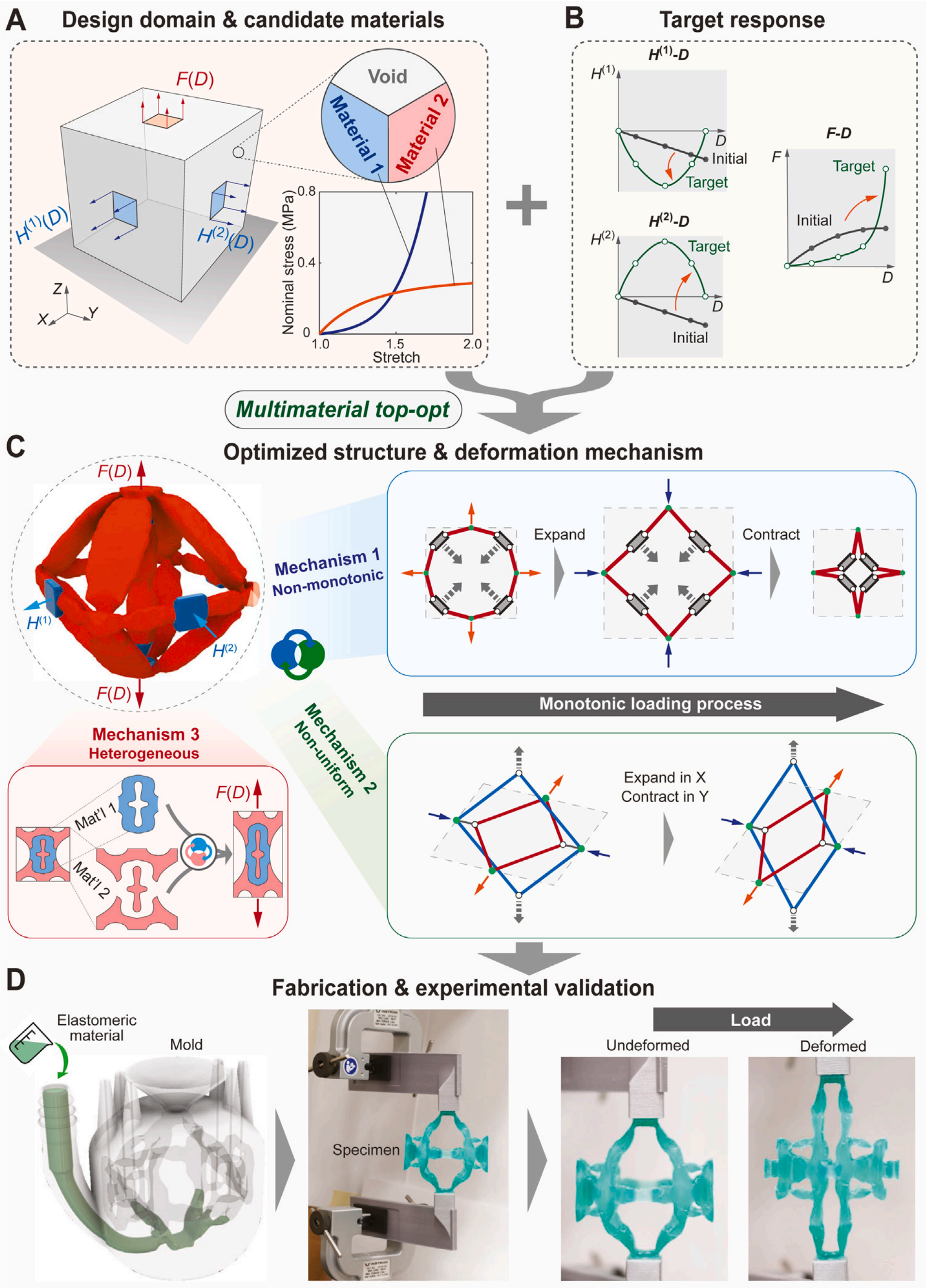

Fig. 1. Programming extreme 3D deformation patterns and $F-D$ relations into metastructures. (A) Design domain, boundary conditions, and candidate nonlinear materials with associated constitutive behaviors; (B) illustration of target and initial design's responses in terms of the applied displacement D versus corresponding force F at control regions and applied displacements D versus induced displacements H at control regions; (C) synthesized 3D structures with spatially coupled 3D mechanisms, unconventional geometries, and multiple materials; (D) proposed hybrid fabrication method combining 3D printing and 3D casting with an elastomeric material and experimental validation.

2. Finite elastostatics with hyperelastic materials

This section introduces the hyperelastic material model used for this study, the associated elastostatics problems, and numerical implementation with the finite element method (FEM).

2.1. Hyperelastic materials

The study focuses on composite structures made of isotropic hyperelastic materials under large deformation. Behaviors of such material can be fully described by a stored-energy density function $W(\boldsymbol{A})$ in terms of invariants or principal stretches of deformation gradient $\boldsymbol{A} := \frac{\partial \boldsymbol{u}}{\partial \boldsymbol{X}}$ (Ogden, 1997), with $\boldsymbol{u}$ being the displacement field and $\boldsymbol{X}$ the location vector of the reference (undeformed) configuration. We use a compressible Ogden model (Feng, Peyraut, & He, 2006; Ogden, 1997) for most of the numerical studies for its simpler form, and we use the Lopez-Pamies (LP) model (Lopez-Pamies, 2010) for one example that will be fabricated and validated experimentally because the LP model can accurately capture the highly nonlinear behavior of the elastomeric material used to manufacture the optimized structure. Details of the LP model and the material will be discussed in Sections 5.3 and 6.

The stored-energy density function of the compressible Ogden model for the kth material is:

$$W^{(k)}\left(\lambda_1,\lambda_2,\lambda_3\right) = \sum_{m=1}^{M} \frac{\mu_m^{(k)}}{\alpha_m^{(k)}} \left(\lambda_1^{\alpha_m^{(k)}} + \lambda_2^{\alpha_m^{(k)}} + \lambda_3^{\alpha_m^{(k)}} - 3\right) + \sum_{m=1}^{M} \frac{\mu_m^{(k)}}{\alpha_m^{(k)}\beta_m^{(k)}} \left(J^{-\alpha_m^{(k)}\beta_m^{(k)}} - 1\right), \tag{1}$$

where λ_i is the ith principal stretch (eigenvalue of $(\boldsymbol{A}^T\boldsymbol{A})^{1/2}$), $J := \det(\boldsymbol{A})$, $\alpha_m^{(k)}$, $\beta_m^{(k)}$, $\mu_m^{(k)}$ are material constants of the kth material. For simplicity, we adopt $M = 1$ and drop the subscript m. Two hyperelastic materials with distinct behaviors are considered herein. Material 1 uses $\alpha^{(1)} = 10$, $\mu^{(1)} = 0.0068$, $\beta^{(1)} = 12$ and represents an initially soft but rapidly stiffening behavior; Material 2 uses $\alpha^{(2)} = -2$, $\mu^{(2)} = -0.3378$, $\beta^{(2)} = 12$ and describes an initially stiff but gradually softening response. The two groups of values represent different types of nonlinearity that can be exploited by the optimized structures to achieve the target mechanical responses. As shown in Fig. 1A, the uniaxial stress–stretch curves of the two materials cross. At the limit of small deformation, the chosen material constants correspond to a Young's modulus and Poisson's Ratio of 0.1 MPa and 0.48 for Material 1, and 1 MPa and 0.48 for Material 2.

2.2. Elastostatics problem and finite element solution

Equilibrium of hyperelastic composite structures can be found by minimization of the total potential energy with respect to the displacement field. To solve this problem, we adopt the standard displacement-based finite element method (FEM) with total Lagrangian formulation and eight-node hexahedral element. In the discretized system with a finite element mesh, the total potential energy is given by:

$$\Pi(\boldsymbol{u}) := \sum_{e} \int_{\Omega_e} W(\boldsymbol{u}_e)\mathrm{d}\boldsymbol{X} - \boldsymbol{f}^{\mathrm{ext}}\boldsymbol{u}, \tag{2}$$

where $\boldsymbol{u}_e$ is the element displacement vector, $\boldsymbol{f}^{\mathrm{ext}}$ is the global external force vector, and Ω_e is the domain of element e in the reference configuration. Equilibrium is attained by the stationary condition:

$$\boldsymbol{r}(\boldsymbol{u}) := \frac{\partial \Pi}{\partial \boldsymbol{u}}(\boldsymbol{u}) = \boldsymbol{f}^{\mathrm{int}}(\boldsymbol{u}) - \boldsymbol{f}^{\mathrm{ext}} = \boldsymbol{0}, \tag{3}$$

where $\boldsymbol{r}$ is the residual vector, and $\boldsymbol{f}^{\mathrm{int}}$ is the internal force vector. This study adopts displacement loading and $\boldsymbol{f}^{\mathrm{ext}} = \boldsymbol{0}$. The loading procedure and structure's responses are modeled quasi-statically.

All design domains in this study are discretized by a 32 × 32 × 32 or 64 × 64 × 64 structured mesh. The nonlinear system (3) is solved by the Newton–Raphson method, and the associated linear systems are solved by a multigrid-preconditioned Generalized Minimal Residual (GMRES) Method (Amir, Aage, & Lazarov, 2014; Barrett et al., 1994; Saad & Schultz, 1986).

3. Inverse design formulation for programming unconventional 3D mechanical responses

3.1. Multimaterial interpolation of stored-energy density functions

This subsection presents the topology optimization formulation for programming 3D nonlinear mechanical responses based on density-based topology optimization (Bendsøe & Kikuchi, 1988; Bendsøe & Sigmund, 2003). The optimization requires a density design field $\rho(\boldsymbol{X}) \in [0,1]$ and a material design field $\xi(\boldsymbol{X}) \in [0,1]$ to parameterize material spatial occupation and material phase at location $\boldsymbol{X}$, respectively. Both design fields are assumed to be piece-wise constant and associated with finite elements. Hence, they can be represented by vector variables $\boldsymbol{\rho}$ and $\boldsymbol{\xi}$, respectively, with the eth entry being the field values within element e. To obtain mesh-independent and near discrete designs, both design variables are filtered and projected to corresponding physical variables $\bar{\boldsymbol{\rho}}$ and $\bar{\boldsymbol{\xi}}$ (Wang, Lazarov, & Sigmund, 2011), which represent the physical structures. For details about the filter and projection, refer to Appendix A.

The physical variables are mapped to the material properties (in this case, stored-energy function density) through a Solid Isotropic Material with Penalization (SIMP)-like interpolation technique (Bendsøe & Sigmund, 2003; Li, Wang et al., 2021; Sigmund, 2001; Zhang, Chi, & Paulino, 2020). The interpolated stored-energy density in element e is

$$W_e\left(\bar{\rho}_e, \bar{\xi}_e, \gamma_e, \boldsymbol{u}_e\right) = \left[\epsilon_\rho + \left(1-\epsilon_\rho\right)\bar{\rho}_e^{p_\rho}\right]\left[\bar{\xi}_e^{p_\xi} W_e^{[1]}\left(\gamma_e, \boldsymbol{u}_e\right) + \left(1-\bar{\xi}_e\right)^{p_\xi} W_e^{[2]}\left(\gamma_e, \boldsymbol{u}_e\right)\right] \tag{4}$$

where $W_e^{[j]}$ is the energy of Material j, p_ρ and p_ξ are penalization parameters, $\epsilon_\rho = 10^{-6}$ is a small number to avoid singularity issues in the state equations, and $\gamma_e \in [0,1]$ is a near-discrete and binary parameter computed by the Heaviside projection of the physical density variable $\bar{\rho}_e$:

$$\gamma_e\left(\bar{\rho}_e\right) = \frac{\tanh\left(\beta_\gamma \rho_{min}\right) + \tanh\left(\beta_\gamma\left(\bar{\rho}_e^{p_\rho} - \rho_{min}\right)\right)}{\tanh\left(\beta_\gamma \rho_{min}\right) + \tanh\left(\beta_\gamma\left(1 - \rho_{min}\right)\right)}, \tag{5}$$

where $\beta_\gamma = 500$ ensures the close-to-discreteness of γ_e, and $\rho_{min} = 0.01$ is the projection threshold. Parameter γ_e is used to interpolate with linear stored-energy density functions at the ground state of each material to stabilize numerical computation through (Wang, Lazarov et al., 2014)

$$W_e^{[j]}\left(\gamma_e, \boldsymbol{u}_e\right) = W_{NL}^{[j]}\left(\gamma_e \boldsymbol{u}_e\right) - W_L^{[j]}\left(\gamma_e \boldsymbol{u}_e\right) + W_L^{[j]}\left(\boldsymbol{u}_e\right), \tag{6}$$

where $W_{NL}^{[j]}$ is Material j's hyperelastic stored energy density given in Eq. (1) or Eq. (15), and $W_L^{[j]}$ is the linear corresponding elastic stored energy density and expressed as

$$W_L^{[j]}(\boldsymbol{u}_e) = \mu^{[j]} \boldsymbol{\varepsilon}(\boldsymbol{u}_e) : \boldsymbol{\varepsilon}(\boldsymbol{u}_e) + \frac{\mu'^{[j]}}{2} \mathrm{tr}^2(\boldsymbol{\varepsilon}(\boldsymbol{u}_e)), \tag{7}$$

where $\boldsymbol{\varepsilon}(\boldsymbol{u})$ is the linearized strain tensor. Parameters $\mu^{[j]}$ and $\mu'^{[j]}$ are Lamé constants of Material j at the ground state. At solid regions, $\gamma_e = 1$ and $W_e^{[j]}\left(\gamma_e, \boldsymbol{u}_e\right) = W_{NL}^{[j]}\left(\boldsymbol{u}_e\right)$; at void regions, $\gamma_e = 0$ and $W_e^{[j]}\left(\gamma_e, \boldsymbol{u}_e\right) = W_L^{[j]}\left(\boldsymbol{u}_e\right)$. Note that void regions have negligible influence on the structural behavior because ϵ_ρ in the interpolated energy (4) is small. For more discussion on this scheme, see Li, Wang et al. (2021).

Based on (4) and (6), the interpolated stored-energy density function (4) recovers the (nonlinear) stored-energy density functions of Material 1 and Material 2 in solid regions ($\bar{\rho}_e = 1$) when $\bar{\xi}_e = 1$ and $\bar{\xi}_e = 0$, respectively, i.e., $W_e\left(\bar{\rho}_e = 1, \bar{\xi}_e = 1, \gamma_e = 1, \boldsymbol{u}_e\right) = W_{NL}^{[1]}(\boldsymbol{u}_e)$ and $W_e\left(\bar{\rho}_e = 1, \bar{\xi}_e = 0, \gamma_e = 1, \boldsymbol{u}_e\right) = W_{NL}^{[2]}(\boldsymbol{u}_e)$.

3.2. Optimization formulation

The study uses multimaterial topology optimization to program a wide range of unique nonlinear responses for 3D composite structures under finite deformations. Specifically, we aim to program the nonlinear force–displacement relation and deformation pattern characterized by displacement history at prescribed locations, because the two responses directly define the functionality of many applications, such as actuators and auxetic metamaterials. In addition, programming force–displacement relation under large deformations allows for the explicit control of the nonlinear structural behavior for the entire loading process. Multimaterial topology optimization simultaneously varies ρ and ξ to minimize a user-defined objective function. For the inverse design problem, we define the objective function as the maximum error between the finite element (FE) simulation response and the prescribed target response along the loading process. When the error is minimized, the corresponding synthesized composite structure (with optimized density and material design fields) accurately achieves the assigned behaviors. Mathematically, the inverse design problem is formulated as:

$$\begin{aligned}
\min_{\boldsymbol{\rho}, \boldsymbol{\xi}} & \left\{ \max_{i \in \{1,\dots,n_1\}} \left[\kappa \sum_{k=1}^{K} \left(\frac{H_k(D^{(i)}, \boldsymbol{\rho}, \boldsymbol{\xi}, \boldsymbol{u}^{(i)}) - H_k^*(D^{(i)})}{\bar{H}} \right)^2 \right.\right. \\
& \qquad \left.\left. + (1-\kappa) \left(\frac{F(D^{(i)}, \boldsymbol{\rho}, \boldsymbol{\xi}, \boldsymbol{u}^{(i)}) - F^*(D^{(i)})}{\bar{F}} \right)^2 \right] + \eta V(\boldsymbol{\rho}) \right\} \\
\text{s.t.} \quad & \boldsymbol{r}_1\left(\boldsymbol{\rho}, \boldsymbol{\xi}, \boldsymbol{u}^{(i)}\right) = \boldsymbol{0}, \quad i = 1, \dots, n_1 \\
& \boldsymbol{r}_2\left(\boldsymbol{\rho}, \boldsymbol{\xi}, \tilde{\boldsymbol{u}}^{(j)}\right) = \boldsymbol{0}, \quad j = 1, \dots, n_2 \\
& V(\boldsymbol{\rho}) - \bar{V} \le 0 \\
& \left\{ \sum_{e=1}^{N} \left[\frac{\frac{1}{v_e} \int_{\Omega_e} \sigma^{VM}\left(\boldsymbol{\sigma}\left(\boldsymbol{\rho}, \boldsymbol{\xi}, \boldsymbol{u}^{(n_1)}\right)\right) \mathrm{d}\boldsymbol{x}}{\bar{\sigma}\left(\boldsymbol{\rho}, \boldsymbol{\xi}\right)} \right]^p \right\}^{\frac{1}{p}} - 1 \le 0 \\
& - s_k\left(\boldsymbol{\rho}, \boldsymbol{\xi}, \tilde{\boldsymbol{u}}^{(n_2)}\right) + \underline{s}_k \le 0, \quad k = 1, \dots, K \\
& \boldsymbol{0} \le \boldsymbol{\rho} \le \boldsymbol{1} \\
& \boldsymbol{0} \le \boldsymbol{\xi} \le \boldsymbol{1}
\end{aligned} \tag{8}$$

where $D^{(i)}$ is the applied vertical displacement at the ith loading step, H_k and H_k^* are the simulation and target induced displacements at control region k, respectively, K is the total number of control regions, $\bar{H}$ is the mean target induced displacement (normalization constant), F and F^* are the simulation and target forces at the loading area, $\bar{F}$ is the mean target input force (constant), V is the structural volume, $\bar{V}$ is the assigned maximum allowable volume, $\kappa \in [0,1]$ is the relative weight of induced displacement and force errors, and η is a (small) volume penalization constant, which ensures removal of superfluous material. Vectors $\boldsymbol{r}_1$ and $\boldsymbol{r}_2$ are residuals of the nonlinear state equations in two different load cases, respectively, with n_1 being the total number of control points for the first (primary) load case, and n_2 being the total number of control points for the second load case. For design scenarios where the loading region and the control region are the same, only the primary load case ($\boldsymbol{r}_1 = 0$) is needed. For scenarios where the loading region and control region are different, we need an auxiliary load case ($\boldsymbol{r}_2 = 0$), with a boundary condition different from that in $\boldsymbol{r}_1$, to impose the minimal structural stiffness constraint. This is realized by requiring the reaction forces of the kth control region s_k to be larger than a minimal value $\underline{s}_k$, when the degrees of freedom corresponding to H at the control region are fixed.

We also include a constraint on maximum von Mises stress (Cheng & Guo, 1997; Cheng & Jiang, 1992) (approximated by the p-norm) at the final (n_1) loading step of the primary load case $\boldsymbol{r}_1$ to prevent the appearance of extremely thin members, excessive deformation, and possible failure (Kundu, Li, & Zhang, 2022; Li, Wang et al., 2021). The von Mises stress is computed using the (interpolated) Cauchy stress, which, based on the interpolated energy density (4), has the following expression (Li, Wang et al., 2021):

$$\boldsymbol{\sigma}\left(\bar{\rho}_e, \bar{\xi}_e, \gamma_e, u_e\right) = \left[\epsilon_p + \left(1-\epsilon_p\right)\bar{\rho}_e^{p_p}\right]\left[\bar{\xi}_e^{p_\xi}\boldsymbol{\sigma}^{[1]}\left(\gamma_e, u_e\right) + \left(1-\bar{\xi}_e\right)^{p_\xi}\boldsymbol{\sigma}^{[2]}\left(\gamma_e, u_e\right)\right] \tag{9}$$

where $\boldsymbol{\sigma}^{(j)}\left(\gamma_e, \boldsymbol{u}_e\right)$ is the Cauchy stress of Material j computed by

$$\boldsymbol{\sigma}^{(j)}\left(\gamma_e, \boldsymbol{u}_e\right) = \boldsymbol{\sigma}_{NL}^{(j)}\left(\gamma_e \boldsymbol{u}_e\right) + \left(1-\gamma_e\right)\boldsymbol{\sigma}_{L}^{(j)}\left(\boldsymbol{u}_e\right) \tag{10}$$

with $\boldsymbol{\sigma}_{NL}^{(j)}$ and $\boldsymbol{\sigma}_{L}^{(j)}$ being the nonlinear and linear parts of the Cauchy stress given by

$$\boldsymbol{\sigma}_{NL}^{(j)}\left(\gamma_e \boldsymbol{u}_e\right) = \frac{1}{J\left(\gamma_e \boldsymbol{u}_e\right)}\boldsymbol{A}\left(\gamma_e \boldsymbol{u}_e\right)\boldsymbol{S}^{(j)}\left(\gamma_e \boldsymbol{u}_e\right)\boldsymbol{A}^T\left(\gamma_e \boldsymbol{u}_e\right) \text{ and } \boldsymbol{\sigma}_{L}^{(j)}\left(\boldsymbol{u}_e\right) = \mathbb{C}^{(j)} : \boldsymbol{\epsilon}\left(\boldsymbol{u}_e\right) \tag{11}$$

In (11), $\boldsymbol{S}$ is the second Piola–Kirchhoff stress of Material j. As in the energy interpolation (4), the interpolated Cauchy stress (9) recovers the Cauchy stress of Material 1 and Material 2 in solid regions ($\bar{\rho}_e = 1$) when $\bar{\xi}_e = 1$ and $\bar{\xi}_e = 0$, respectively. For void regions, the Cauchy stress is negligible as ϵ_ρ is small.

In addition to interpolating Cauchy stress, material strength $\bar{\sigma}$ also needs to be interpolated as

$$\bar{\sigma}\left(\bar{\rho}_e, \bar{\xi}_e\right) = \left[\epsilon_q + \left(1-\epsilon_q\right)\bar{\rho}_e^{q_\rho}\right]\left[\bar{\xi}_e^{q_\xi}\bar{\sigma}^{[1]} + \left(1-\bar{\xi}_e\right)^{q_\xi}\bar{\sigma}^{[2]}\right] \tag{12}$$

where $\bar{\sigma}^{(j)}$ is the prescribed von Mises stress limit for Material j, and $\epsilon_q = 10^{-6}$. The penalization parameters are chosen as $q_\rho = p_\rho - 0.5$ and $q_\xi = p_\xi - 0.5$. As in the interpolated Cauchy stress (9), the interpolated limit $\bar{\sigma}$ becomes $\bar{\sigma}^{[1]}$ and $\bar{\sigma}^{[2]}$ in solid regions ($\bar{\rho}_e = 1$) when $\bar{\xi}_e = 1$ and $\bar{\xi}_e = 0$, respectively. For more discussions on the stress constraint and its impact on (other) optimized designs, readers are referred to Kundu et al. (2022) and Li, Wang et al. (2021).

We note that this study focuses on programming nonlinear force–displacement relations and deformation patterns under applied displacement in one direction. However, the formulation can be extended to program multiaxial responses. This can be realized in the objective function by either including the response errors from multiple loading directions as a weighted sum or applying the maximum operator on response errors from those directions.

3.3. Sensitivity analysis and solution algorithm

The optimization problem (8) is solved by a gradient-based algorithm, which requires the analytical expression of sensitivities (gradients) of objective and constraint functions with respect to the two design variables. Here, we use the adjoint method (Bendsøe & Sigmund, 2003; Li, Wang et al., 2021) to compute the sensitivity. For a general scalar function $\phi(\boldsymbol{\rho}, \boldsymbol{\xi})$ (can represent objective or constraint functions), its gradients with respect to design variable $\boldsymbol{y}$ (representing either $\boldsymbol{\rho}$ or $\boldsymbol{\xi}$) are obtained by:

$$\frac{\partial \phi}{\partial y_e} = \left.\frac{\partial \phi\left(\bar{\boldsymbol{\rho}}, \bar{\boldsymbol{\xi}}, \boldsymbol{u}^{(i,j)}\right)}{\partial y_e}\right|_u + \boldsymbol{\zeta}^T \frac{\partial \boldsymbol{r}_j\left(\bar{\boldsymbol{\rho}}, \bar{\boldsymbol{\xi}}, \boldsymbol{u}^{(i,j)}\right)}{\partial y_e} \tag{13}$$

where $\boldsymbol{\zeta}$ is the adjoint vector, and $\boldsymbol{u}^{(i,j)}$ denotes the displacement vector at load step i of the jth load case. The $\boldsymbol{\zeta}$ is obtained by solving the linear adjoint system:

$$\boldsymbol{K}^T\left(\bar{\boldsymbol{\rho}}, \bar{\boldsymbol{\xi}}, \boldsymbol{u}^{(i,j)}\right)\boldsymbol{\zeta} = -\frac{\partial \phi\left(\bar{\boldsymbol{\rho}}, \bar{\boldsymbol{\xi}}, \boldsymbol{u}^{(i,j)}\right)}{\partial \boldsymbol{u}^{(i,j)}} \tag{14}$$

with $\boldsymbol{K}\left(\bar{\boldsymbol{\rho}}, \bar{\boldsymbol{\xi}}, \boldsymbol{u}^{(i,j)}\right) := \partial^2 \Pi(\bar{\boldsymbol{\rho}}, \bar{\boldsymbol{\xi}}, \boldsymbol{u}^{(i,j)})/\partial \boldsymbol{u}^2$ being the tangent stiffness matrix evaluated at ith load step of load case j.

Based on the expressions of sensitivity, the optimization problem is solved by the gradient-based Method of Moving Asymptotes (Svanberg, 1987), where the min–max problem (8) is equivalently transformed into a bound formulation (Olhoff, 1989) to accommodate for the non-differentiability. The optimization is ended when the change of design variable becomes smaller than a tolerance or the maximum step is reached.

All implementations and computations are carried out on Matlab 2020b (MATLAB, 2020). To improve the fitting accuracy of the inverse design, we adopt continuation schemes for the penalization parameters and projection parameters of the SIMP interpolation of $\bar{\rho}$ and $\bar{\xi}$. The penalization parameter of $\bar{\rho}$ is increased from 1 to 3 at an interval of 0.5 every 20 optimization steps starting from the 60th step, after which the penalization parameter of $\bar{\xi}$ is increased from 1 to 3 with the same fashion. Both parameters reach 3 at the 220th step, where the projection parameter of $\bar{\rho}$ starts to increase from 1 by a factor of 2 every 20 steps until reaching 64 at 340th step. Then, the projection parameter of $\bar{\xi}$ increases from 1 with the same pattern and reaches 64 at the 460th step. The maximum number of optimization steps is set to 500. To reduce the computational cost, we first carry out the above optimization

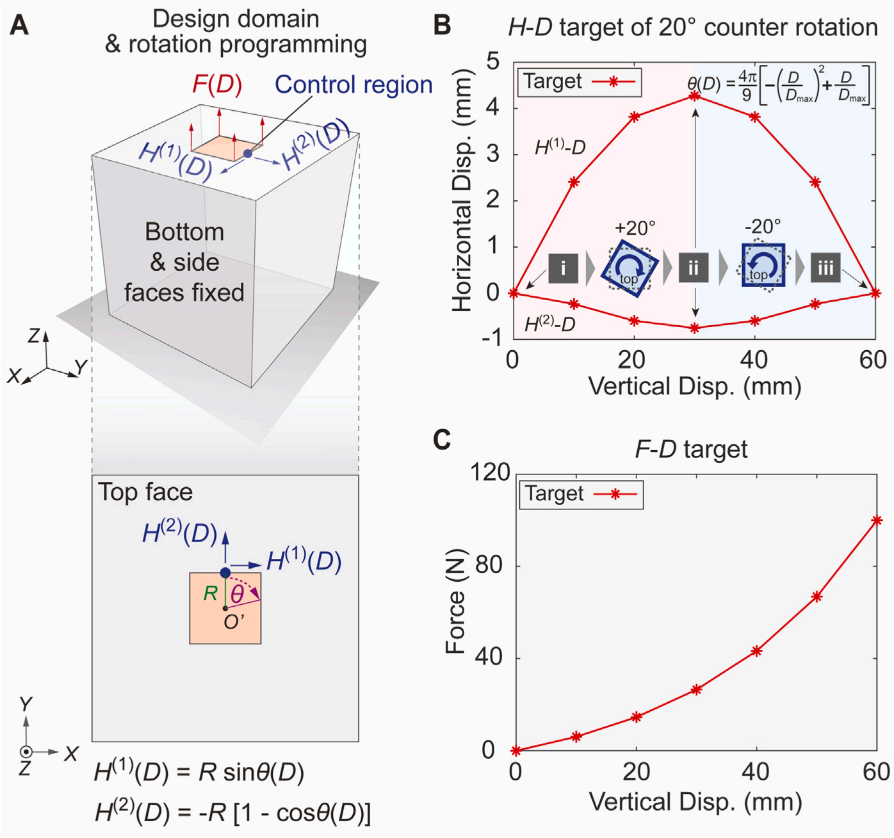

Fig. 2. Problem setup for programming 3D rotation-then-counter-rotation behavior into structures. (A) Design domain, boundary conditions, and control regions; (B) target $H-D$ relation of 20° rotation-then-counter-rotation (a sequential clockwise then counter-clockwise rotation in the horizontal plane); (C) target stiffening $F-D$ relation.

and obtain the optimized result with a 32 × 32 × 32 mesh. The result is then interpolated to a 64 × 64 × 64 mesh, which serves as the initial guess and is optimized for additional 50 steps using the 64 × 64 × 64 mesh to obtain the final result. The computation is carried out on a workstation with AMD Ryzen Threadripper 3970X 32-Core processor (3.69 GHz). The computation time for the 500-step 32 × 32 × 32 mesh optimization is approximately two to three days, and that for the 50-step 64 × 64 × 64 mesh takes approximately three days.

4. Programming non-monotonic rotation-then-counter-rotation behavior under monotonic vertical loading

This section introduces a novel rotation-then-counter-rotation response and elucidates its underlying mechanisms. Precise realization of such non-monotonic rotation behavior with prescribed $F-D$ response can be challenging, as the structural geometry, material distribution, and driving mechanisms that collectively produce this 3D non-monotonic mechanical behavior can be highly complex. We remark that rotation-then-counter-rotation has been attained under vertical compression with cellular structures that exploit the buckling of slender members to switch the rotation direction (Goswami et al., 2020). Yet, precise programming of 3D non-monotonic rotation behavior under tension loading with prescribed $F-D$ relation (the case herein) has not been explored yet.

Using the proposed inverse design framework (8), we synthesize a 3D multimaterial structure that exhibits a sequential clockwise then counter-clockwise rotation in the horizontal plane and rapid stiffening $F-D$ response under monotonic vertical tension loading. We use the design domain and boundary conditions in Fig. 2A. The domain is a $200 \times 200 \times 200$ mm^3 cube with the bottom and four side surfaces (those with outward normal $+X$, $-X$, $+Y$, and $-Y$) fixed. The structure is loaded vertically by applied displacement D at the square red region at the top (no constraints for displacements in X–Y plane). The structural rotation in the horizontal plane (X–Y plane) is programmed through the relation between rotation angle and applied displacement ($\theta - D$). The rotation angle (θ) is defined through the horizontal induced displacements of the small control region at the loading area (i.e., the dark blue point in Fig. 2A) relative to the center of the top face O'. We aim to attain a rotation-then-counter-rotation behavior with which the structure would sequentially rotate clockwise then counter-clockwise by 20° under monotonic D. We use a quadratic $\theta - D$ relation of $\theta(D) = \frac{4\pi}{9}(-\frac{D^2}{D_{max}^2} + \frac{D}{D_{max}})$, which corresponds to relations of induced-to-applied displacements, $H^{(1)} - D$ and $H^{(2)} - D$, in X and Y directions, respectively, as shown in Fig. 2B. Additionally, the $F-D$ relation is programmed with a stiffening target response

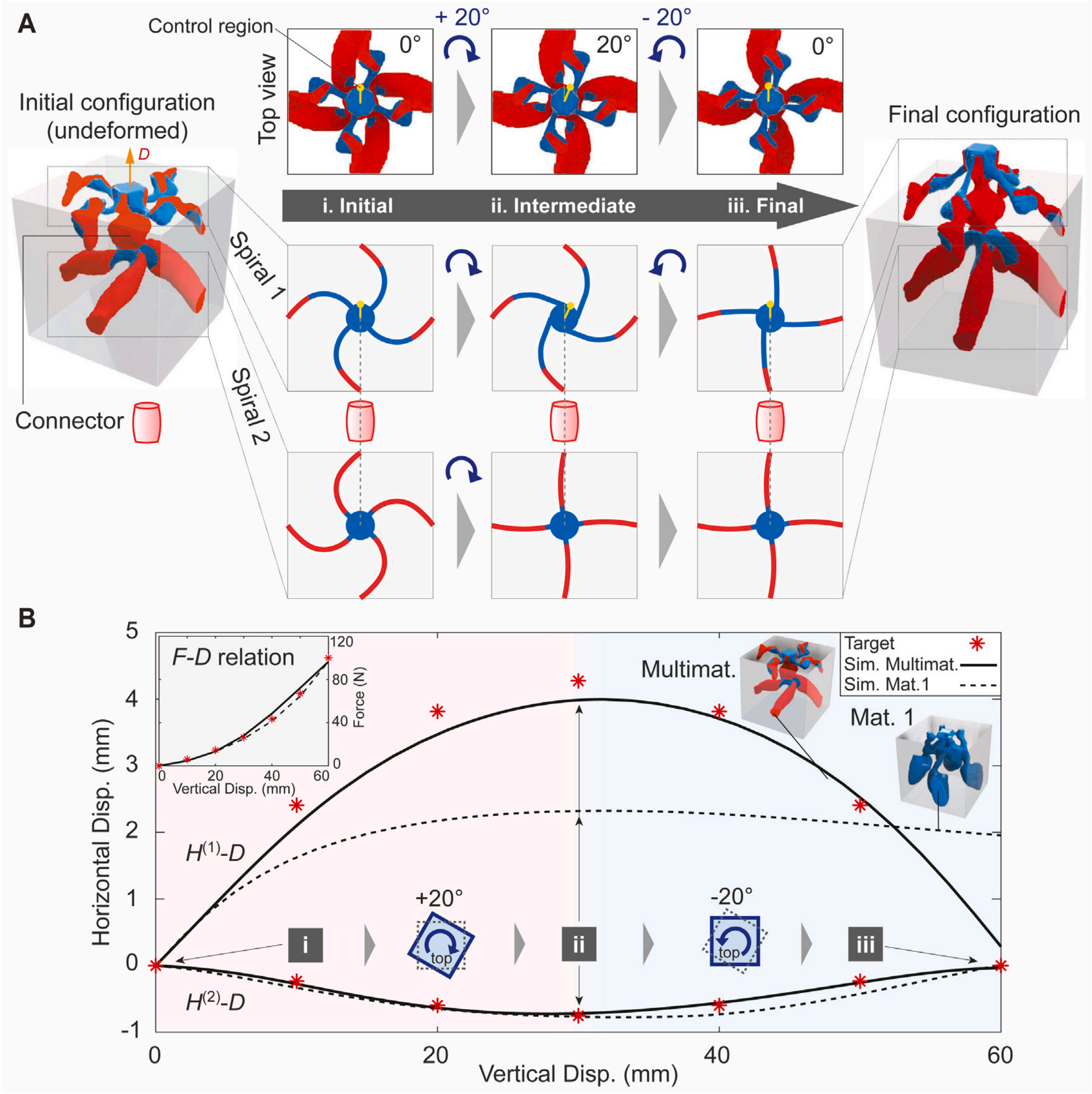

Fig. 3. Synthesized multimaterial structure and mechanism of programmed rotation-then-counter-rotation response under monotonic loading. (A) Optimized multimaterial designs at initial (undeformed), intermediate, and final configurations with corresponding simplified models of two spiral components (controlled region is highlighted with a yellow dot); (B) simulation versus target $H^{(1)}-D$, $H^{(2)}-D$, and $F-D$ (inset) relations of the multimaterial and single material (Mat.1) structures. The Mat.1 structure is optimized with the same setup as the multimaterial structure but uses Material 1 alone.

(Fig. 2C), which shows a similar stiffening trend as Material 1's stress–stretch response (Fig. 1A) and hence is expected to introduce Material 1 in the final design. However, sole reliance on Material 1 may fail to accurately achieve the large rotation as Material 1 is extremely soft at low strain and could fail to initiate the large deformation. Therefore, a multimaterial design should be favored over single-material ones to accurately achieve both the large target counter rotation and the target stiffening $F-D$ curve.

The inverse design framework produces a multimaterial structure, as shown in Fig. 3A, with the structure's simulation $H-D$ and $F-D$ responses shown in Fig. 3B, demonstrating precise realization of both the non-monotonic rotation and stiffening behaviors. From the 3D initial configuration of Fig. 3A, the structure consists of top and bottom spiral components (labeled as Spirals 1 and 2, respectively) connected through a thick vertical member (labeled as connector). Both spirals possess two materials and attach to the side supports at different heights, and the connector is made of Material 2 alone. Importantly, the pattern of Spiral 1 is counter-clockwise while that of Spiral 2 is clockwise, as shown in Fig. 3A. The reversed spiral patterns and special material distributions constitute the mechanisms driving the counter-rotation and stiffening response.

To further explain the two-spiral mechanism, we show the top views of the structure at the initial, intermediate, and final configurations. Correspondingly, we introduce simplified representations of the two spirals and connector shown in Fig. 3A, in which the branches and centers can be interpreted as curved beams and rigid plates, respectively, and the red and blue colors indicate the material types. At the initial loading stage, the external force is mainly transmitted to Spiral 2 through the stiff connector, and little force is carried by Spiral 1. This is because Spiral 2's vertical stiffness is significantly larger than Spiral 1's due to the thicker members, dominant occupation of Material 2 (the initially stiffer material), and the tilted vertical alignment of the branches. When pulled up, the spiral geometry causes Spiral 2 to rotate clockwise, which drives Spiral 1 to rotate in the same direction through the stiff connector. At this stage, Spiral 1 cannot resist the driving torque from Spiral 2 and rotates as a follower because Spiral 1's rotational stiffness is significantly lower than Spiral 2's. The small stiffness of Spiral 1 is due to the slender geometry and largely horizontal orientations of the branches with a substantial portion of Material 1 (the initially softer material). As loading approaches the intermediate stage, Spiral 2 branches straighten under rotation and form a larger vertical angle due to the applied displacement, resulting in more axial deformation whilst maintaining large rotational stiffness. In the mean time, the vertical applied displacement has considerably raised the axial stretch and force of Spiral 1 branches. Coupled with the spiral geometry, the increased axial force triggers a counter-clockwise rotation of Spiral 1. Hence, at the intermediate stage, Spiral 1 drives the rotation while Spiral 2 serves as a rotational support as it remains relatively static in the horizontal plane. When loaded further, the rising axial force in Spiral 1 branches continues generating counter-clockwise rotation till the final stage where the branches straighten and rotation ceases. The complete deformation process of this non-monotonic rotation-then-counter-rotation behavior under monotonic vertical loading is given in Supplementary Video S2.

As indicated in the above analysis, the sequential clockwise then counter-clockwise structural rotation is caused by the asynchronous activation of two torques in opposite directions with different magnitudes. The asynchrony is mechanically facilitated by the optimized geometry and material distribution, as well as the large behavioral discrepancy between the two materials. During the first half of loading, Spiral 2's stiffness significantly outweighs Spiral 1's, and hence, Spiral 2's rotation drives Spiral 1 and overall structure to rotate clockwise. During the second half of loading, Spiral 2 branches straighten and cease to rotate further while Spiral 1 starts to rotate counter-clockwise as its axial force grows rapidly due to Material 1's stiffening behavior. This signals a shift in the driver for rotation from Spiral 2 to Spiral 1, producing the subsequent counter-rotation.

The asynchronous activation is fundamentally related to material heterogeneity and, hence, inaccessible in a single-material structure. To demonstrate this, we plot the simulated behaviors of the structure optimized with a single material (i.e., with Material 1 alone) in Fig. 3B. The pure Material 1 structure fails to achieve the counter-rotation behavior, although it attains the stiffening $F-D$ response (owing to Material 1's stiffening behavior). The structure optimized with Material 2 alone fails to converge and cannot form an effective geometry. The comparison confirms the unique advantage of expanded design space and improved inverse design performance from using multiple materials with dissimilar properties (Li, Wang et al., 2021).

5. Unconventional lateral expansion–contraction behaviors under monotonic loading

In this section, we explore 3D multimaterial structures with unique lateral expansion and contraction behaviors under monotonic vertical loading and elucidate the driving mechanisms. These expansion/contraction responses can be viewed as fundamental generalization of auxetic behaviors. Thus far, most established auxetic metamaterials/metastructures share two major features: (1) the lateral expansive behaviors in the two principal directions are identical, and (2) the lateral deformation is unidirectional (no switch from expansion to contraction or vice versa) under monotonic loading. More recently, non-monotonic and transversely uniform lateral deformation is precisely realized by orthogonally assembled 2D compliant mechanisms with special geometries (Farzaneh, Pawar, Portela, & Hopkins, 2022). Assembly-free 3D continuum metamaterials/metastructures that show both direction-dependent and non-monotonic lateral deformation are not yet realized.

To achieve unconventional lateral behaviors, we adopt the design setup and boundary conditions in Fig. 4A, where a displacement D is applied at the top (red region), and the induced displacements normal to the surface of the two control regions (blue regions), i.e., $H^{(1)}-D$ and $H^{(2)}-D$ relations, are programmed. As indicated in Fig. 4A, throughout this section, $H^{(1)}$ represents the X displacement of the control region on the surface with normal X, and $H^{(2)}$ represents the Y displacement of the control region on the surface with normal Y. The $F-D$ relations are omitted. We aim to achieve direction-dependent expansion and contraction, sequential expansion–contraction, and combined direction-dependent and sequential expansion–contraction behaviors. The target $H^{(1)}-D$ and $H^{(2)}-D$ relations corresponding to these behaviors are shown in Fig. 4B. Under monotonic vertical loading, Structure 1 contracts in the X direction and expands in they Y direction by 16 mm (20% of domain size) with a constant displacement rate; Structure 2 sequentially expands then contracts with the same rate in X and Y directions by 8 mm (10% of domain size); Structure 3 sequentially contracts then expands in the X direction and sequentially expands then contracts in the Y direction by 8 mm (10% of domain size). Precise realization of these unconventional expansion/contraction responses could be highly challenging due to uncharted mechanisms and potentially complex geometries.

5.1. Direction-dependent expansion–contraction

Using the multimaterial topology optimization framework and Structure 1 $H^{(1)}-D$ and $H^{(2)}-D$ targets, we obtain the direction-dependent contraction–expansion structure shown in Fig. 5A. The structure possesses branches with different sizes and is dominantly occupied by Material 2 with limited proportion of Material 1. As shown in Fig. 5B, the structure accurately achieves the linear target contraction in X and expansion in Y directions. The final lateral expansion and contraction are 32 mm (two sides), which is 40% of the domain size. The direction dependence is mainly produced by the special orientation and location of the branches. As shown in Fig. 5A, the structure features four inclined members each with two branches in the X–Z plane, and these members are connected to an encircling ring in the lateral (X–Y) plane. The two groups of members form a dual-rhombus mechanism as illustrated in Fig. 5C,

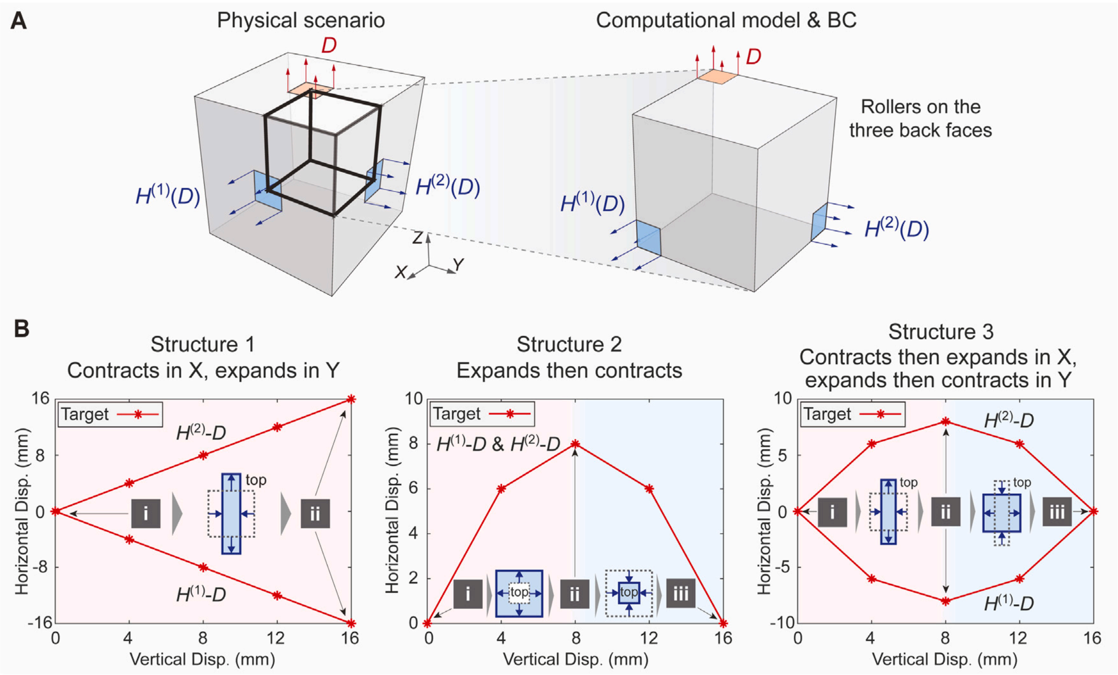

Fig. 4. Problem setup for programming complex lateral expansion/contraction responses under monotonic loading. (A) Physical scenario, design domain, and boundary conditions; (B) target $H - D$ relations for three different expansion/contraction behaviors; Structure 1 contracts in X and expands in Y; Structure 2 sequentially expands then contracts uniformly; Structure 3 contracts then expands in X and expands then contracts in Y directions.

where black straight bars represent the inclined members (Rhombus 1), and gray curved bars represent the ring (Rhombus 2). When loaded vertically, the inclined members (Rhombus 1) extends in Z and contracts in X as a result of the rhombus geometry, which in turn drives the ring (Rhombus 2) to contract in X and expands in Y. The dual-rhombus mechanism is depicted in Fig. 5D through the two groups of sliced views of the undeformed and deformed configurations from side and top perspectives. The sliced view of X–Z plane corresponds to Rhombus 1, and the sliced view of X–Y plane corresponds to Rhombus 2. The large induced lateral deformation of $H^{(1)}$ and $H^{(2)}$ can be observed in the deformed configuration, in which the gray square boxes indicate the boundaries of undeformed configuration. The complete deformation process of this direction-dependent expansion–contraction is illustrated in Supplementary Video S3. Note that while highlighting the driving force of direction-dependent expansion–contraction, the dual-rhombus model (Fig. 5C) omits many details of the 3D structure and is highly simplified. For example, the hinges connecting the bars in the model are substantial simplifications of the solid regions in the actual structure that deform by flexure. In addition to the dual-rhombus system, the structure also feature two vertical members (Fig. 5A) connecting the top and bottom. These vertical members provide vertical stiffness and resistant during vertical loading and are relatively independent from the expansion–contraction behavior. Besides the governing dual-rhombus mechanism, the shape, size, and material composition of each member are finely optimized to precisely realize the constant target expansion–contraction rate.

5.2. Sequential expansion–contraction

Next, we design a structure that sequentially expands then contracts by 8 mm on each side (10% of domain size) under monotonic loading. We use Structure 2 target of Fig. 4B, where the induced displacements $H^{(1)}$ and $H^{(2)}$ are quadratic functions of the applied displacement D. The targets represent a sequential expansion–contraction with the final width of the structure recovering the initial undeformed value. Such non-monotonic self-recovering deformation under monotonic stimulation can benefit intelligent control that requires reversed actions under excessive stimulation.

The optimized multimaterial structure at initial, intermediate, and final configurations is shown in Fig. 6A. The corresponding simulation (and target) responses are plotted in Fig. 6B, which demonstrates precise realization of the sequential expansion–contraction behavior. As shown in Fig. 6A, the structure features three major components: the four inclined members connected to the loading area, the slender ring structure in the horizontal plane, and the internal vertical member. Coupled deformation of the three accurately produces the target behavior. To illustrate the underlying mechanism, we study structural configurations at the initial, intermediate, and final stages from top perspective in Fig. 6C. Three corresponding zoomed-in and sliced (by cut plane 2 of Fig. 6A) views of one quarter highlights the driving mechanism, which is represented by a simplified bar-and-block model in

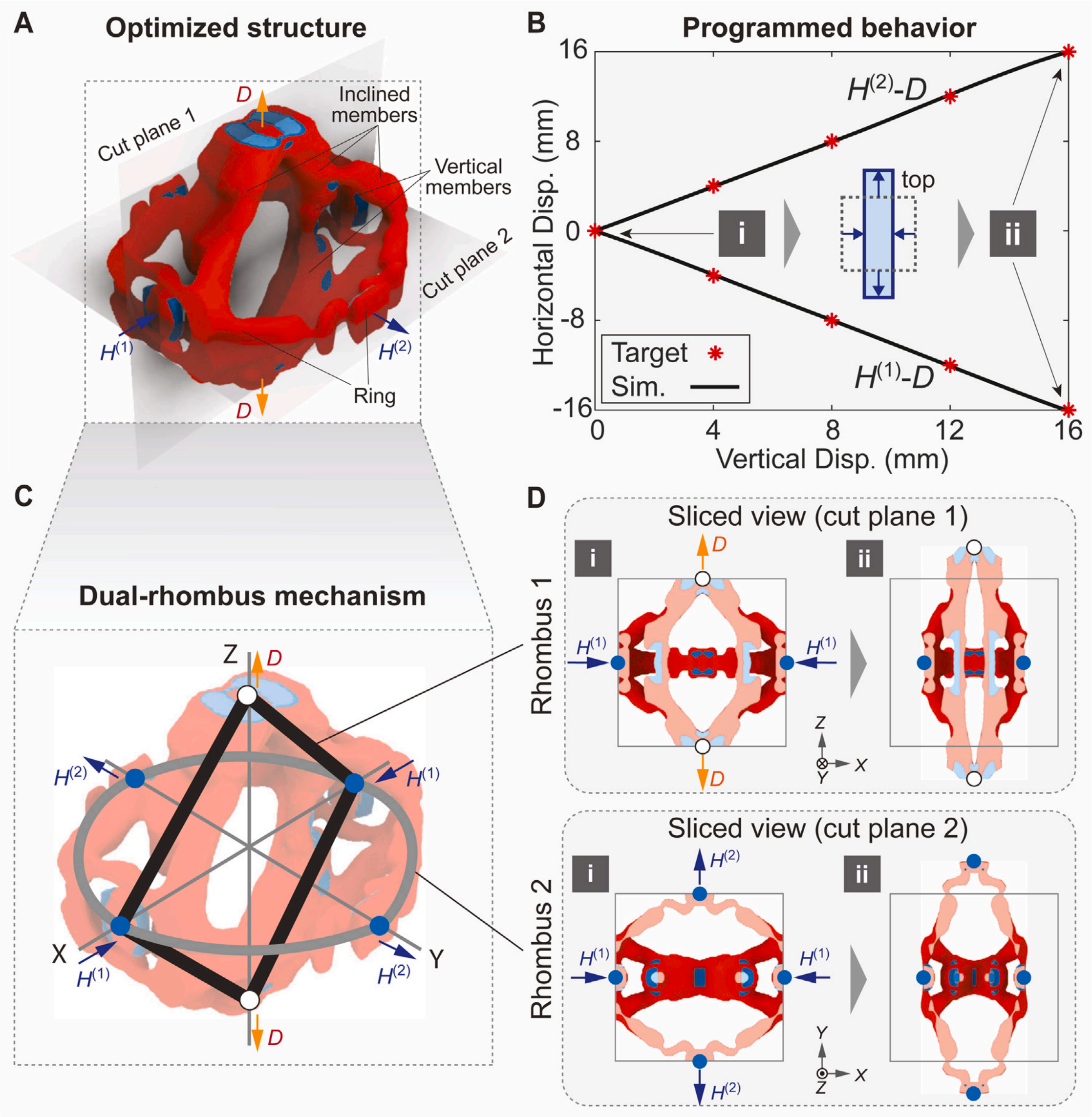

Fig. 5. Synthesized structure that contracts in X and expands in Y directions. (A) Optimized multimaterial design (two cut planes correspond to the two sliced views in (D)); (B) target versus simulation $H^{(1)} - D$ and $H^{(2)} - D$ responses; (C) simplified dual-rhombus mechanism; (D) sliced views of the structure corresponding to the two rhombuses in the X–Z (cut plane 1) and X–Y planes (cut plane 2).

Fig. 6C. The bars represent the two ring branches (in the zoomed-in view), and the block represents the cross-section of the inclined member at the horizontal plane. When loaded vertically, the inclined members contract in the diagonal directions of X–Y plane as a result of geometry and kinematics, and squeeze and bend the ring. The slender ring then buckles and pushes out the control regions, causing the structure to expand as indicated in the initial configuration of Fig. 6C. The expansion reaches maximum at the intermediate stage (Stage ii) where the ring branches form an approximately 90° angle to the diagonal track of inclined members. This configuration is shown in the intermediate configuration of Fig. 6C. When loaded further, the inclined members continue to contract, form an obtuse angle to the ring branches, and pull the branches inward. This mechanism causes the structure to contract as shown in the final configuration of Fig. 6C. Therefore, the special (and optimized) geometry and kinematics drive the sequential expansion and contraction under monotonic loading. The complete deformation process is given in Supplementary Video S4.

As indicated in the simplified model (Fig. 6C), to initiate the expansion, the horizontal angle between the ring branches and the domain boundary $\alpha \in [0, 45°]$. Also, because the stiffness of the axially stretching inclined members significantly exceeds the bending ring, kinematics is mainly imposed unidirectional from the inclined members to the ring. Besides, the internal vertical member provides the vertical stiffness and resistance to loading and is relatively independent from the inclined member-ring system.

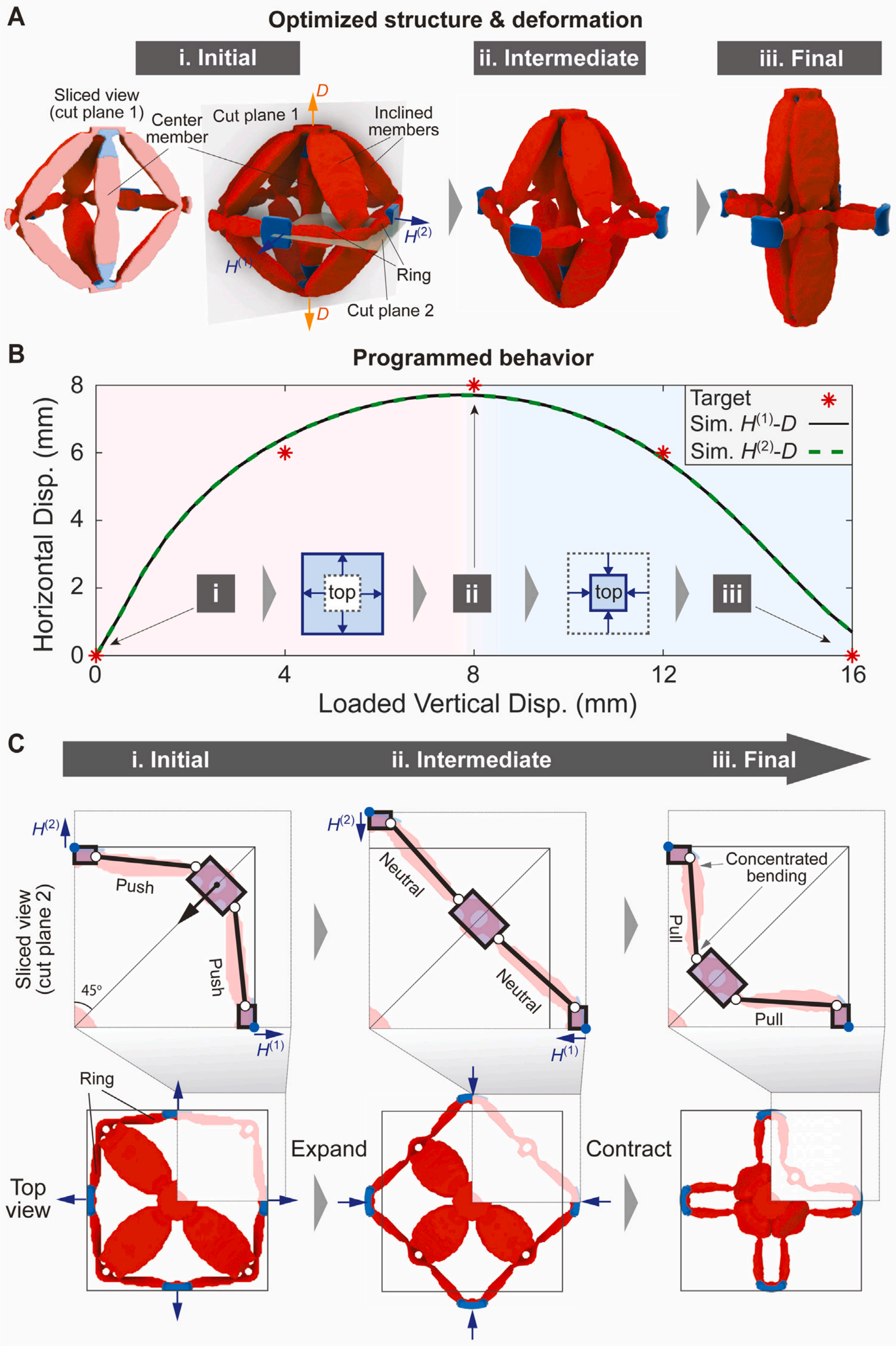

Fig. 6. Synthesized structure that sequentially expands then contracts in horizontal dimensions under monotonic loading. (A) Optimized multimaterial design at initial (undeformed), intermediate, and final configurations; (B) target versus simulation $H^{(1)} - D$ and $H^{(2)} - D$ responses; (C) simplified sequential push-pull mechanism and top views of the structure at three loading stages with zoomed-in sliced view at cut plane 2.

5.3. Direction-dependent and sequential expansion–contraction

In this subsection, we combine the defining features of the two previous structures to design direction-dependent and sequential expansion–contraction behavior. Further, we fabricate the optimized structure with Polydimethylsiloxane (PDMS) elastomer and validate its programmed behavior experimentally. We use Structure 3 target of Fig. 4B, which includes quadratic functions of applied displacement D with opposite signs. The target indicates a sequential contraction then expansion in X direction and sequential expansion then contraction in Y under monotonic loading. At the final stage, the structural widths in X and Y directions recover their undeformed values. To ease subsequent fabrication, we consider one material (instead of two) in the inverse design. Also, as the nonlinear behaviors of PDMS can be accurately captured by the Lopez-Pamies (LP) model (Li et al., 2022), we will use the LP model (instead of Ogden model) for this structure. The stored-energy density function of compressible LP model is (Lopez-Pamies, 2010)

$$W\left(I_1\right)=\sum_{m=1}^{M}\frac{3^{1-\alpha_m}}{2\alpha_m}\mu_m\left(I_1^{\alpha_m}-3^{\alpha_m}\right)-\left(\sum_{m=1}^{M}\mu_m\right)\ln J+\frac{1}{2}\mu'(J-1)^2, \tag{15}$$

where I_1 is the first principal invariant of the right Cauchy–Green deformation tensor, i.e., $\boldsymbol{A}^T\boldsymbol{A}$. This study uses a two-term model, i.e., $M=2$, with coefficients $\alpha_1=2.9798$, $\mu_1=0.0276$, $\alpha_2=-0.0783$, and $\mu_2=0.1478$. These values are obtained based on uniaxial tests of PDMS with a 20:1 base-agent ratio (Li et al., 2022) (see Appendix B for experimental and fitted stress–stretch relations of PDMS). For the compressibility parameter, this study uses $\mu'=8.77$, which corresponds to a 0.48 Poisson's ratio in the small deformation limit and serves to prevent finite element locking.

Using the LP model, we obtain the optimized structure exhibiting direction-dependent and sequential expansion–contraction behaviors as shown in Fig. 7. The initial, intermediate, and final configurations of the structure are shown in Fig. 7A, and the corresponding simulation responses are shown in Fig. 7B, demonstrating accurate realization of prescribed responses. As shown in Fig. 7A, the structure features many intricately connected branches with different sizes, shapes, and orientations. Albeit highly complex, the structure retains the horizontal ring structure (not perfectly in middle X–Y plane) and inclined members as shown in Fig. 7A and C. In addition, the structure forms four vertical members largely aligned in Z direction as indicated in Fig. 7A. The vertical members are connected to the ring through slender rods (shown in Fig. 7A and C), which are referred to as fulcrum members (elaborated in the following discussion). Together, these intricately connected members produce the designed behavior.

To further explain the underlying mechanism, we investigate the initial, intermediate, and final configurations as shown in Fig. 7C, with a zoomed-in view of one quarter. The black arrow pairs indicate tension or compression in the members. Based on the zoomed-in view, we first analyze the sequential contraction–expansion of $H^{(1)}$ (X direction). Upon initial loading, both the inclined members and vertical members contract because of a rhombus mechanism (similar to the first expansion–contraction structure) and produces the motion shown in the first zoomed-in view in Fig. 7C. The motion toward the center (negative X direction) pulls the ring member and $H^{(1)}$ control region inward and causes the structure to contract in X direction as evidenced in the zoomed-in plots of the initial and intermediate stages of Fig. 7C. During this process, the ring member connecting to $H^{(1)}$ control region translates with negligible rotation and internal deformation owing to the similar magnitudes and directions of displacements imposed from the inclined and vertical (and fulcrum) members. The structural contraction in X reaches maximum at the intermediate stage (Stage ii) because the axially stretched vertical member has displaced to near the loading axis (Z axis) and ceases producing X-direction motions. Further loading in Z only yields axial stretch for the vertical member. By contrast, at Stage ii, the inclined member remains far from the Z axis. As a result, further loading in Z continues to produce considerable horizontal displacement for the inclined member. The large discrepancy in horizontal displacements of the inclined and vertical members, together with the steady fulcrum member, generates a lever effect on the ring branch connecting the $H^{(1)}$ control region. The lever effect is depicted in the Stage ii zoomed-in view in Fig. 7C. Motion of the inclined member applies the "effort", the steady fulcrum member provides the "support", and the ring member serves as the "beam". This lever mechanism causes the ring member to rotate significantly and pushes $H^{(1)}$ control point out (positive X direction), which leads to the expansion in X direction during the second half of loading. The large rotation of the ring branch and steadiness of the vertical member are evidenced in the Stage iii zoomed-in view of Fig. 7C, where the ring branch rotates counter-clockwise by approximately 20°, and location and orientation of the fulcrum remains largely unchanged from Stage ii. The deformation process of the two-stage response is given in Supplementary Video S1.

Note that the contraction and expansion mechanisms of $H^{(1)}$ are fundamentally different in that contraction is caused by the shrinking rhombus (formed by vertical and inclined members) taking place mostly in the X–Z plane and requiring similar magnitudes and directions for horizontal displacements; whereas the subsequent expansion mechanism forms mainly in the horizontal (X–Y) plane and demands large discrepancy of horizontal displacement magnitudes to trigger the lever effect. Hence, there is a mechanism transition, and the overall mechanism for the sequential contraction–expansion of $H^{(1)}$ is asynchronous. A necessary condition for the asynchrony is the large difference in initial locations and orientations of the vertical and inclined members. Because the vertical member is significantly closer to the Z axis, its horizontal movement diminishes at the intermediate stage while the inclined member is displacing. Importantly, the switch from contraction to expansion requires highly coupled 3D deformation unavailable in 2D or pseudo 3D structures.

In the Y direction, the sequential expansion–contraction of $H^{(2)}$ is produced by a push-pull mechanism similar to the previous structure. The mechanism is also illustrated in the three zoomed-in plots of Fig. 7C. The continuous horizontal contraction of the inclined members first pushes out then pulls in the control region of $H^{(2)}$. This mechanism differs fundamentally from the $H^{(1)}$ mechanism and is generated by a different part of the structure. Hence, the overall mechanism of the entire structure is heterogeneous.

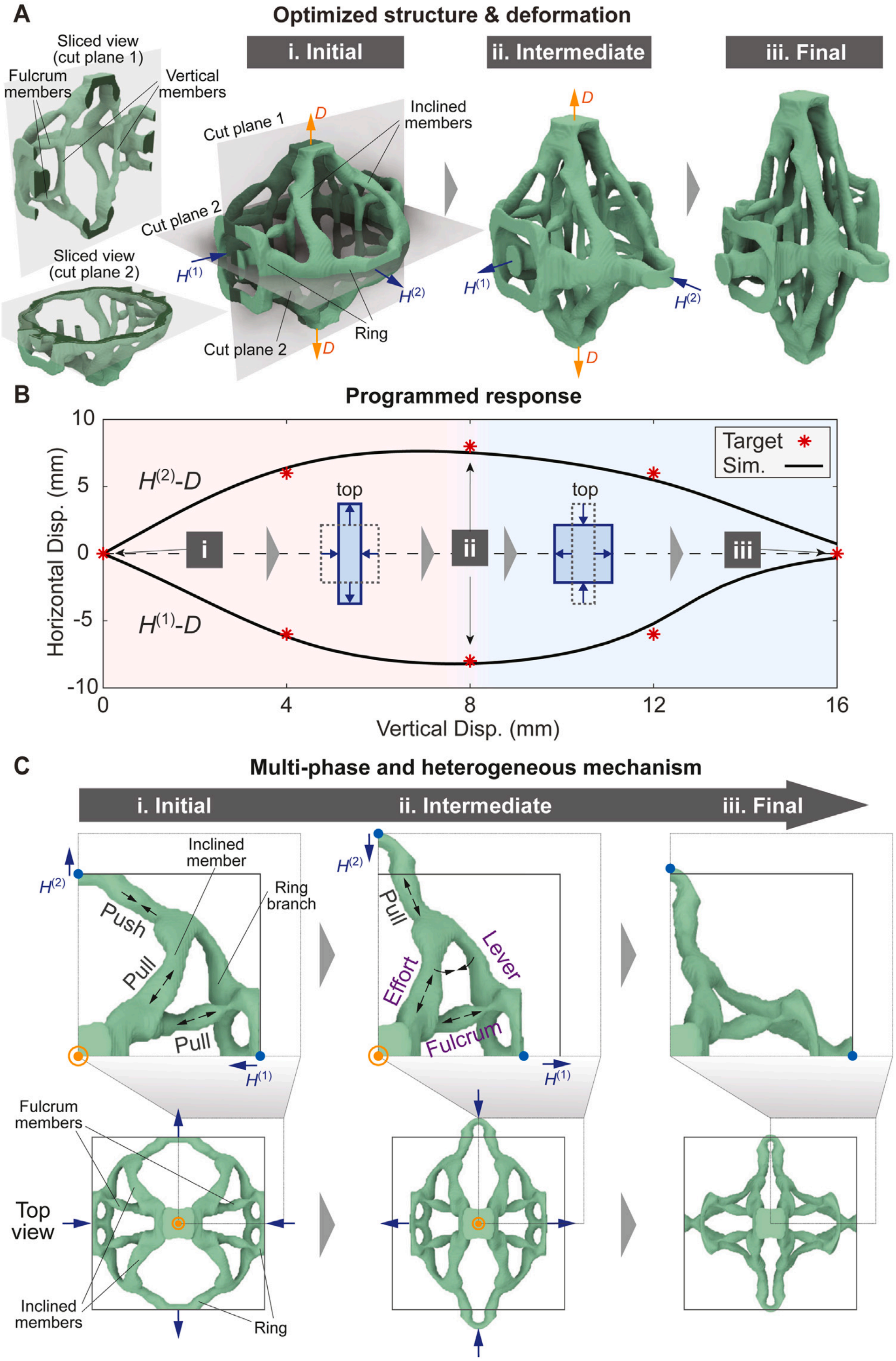

Fig. 7. Optimized structure that sequentially contracts then expands in X and sequentially expands and contracts in Y directions under monotonic loading. (A) Optimized design at initial (undeformed), intermediate, and final configurations; (B) target versus simulation $H^{(1)} - D$ and $H^{(2)} - D$ responses; (C) multi-phase and heterogeneous mechanisms and top views of the structure at the three loading stages with zoomed-in views.

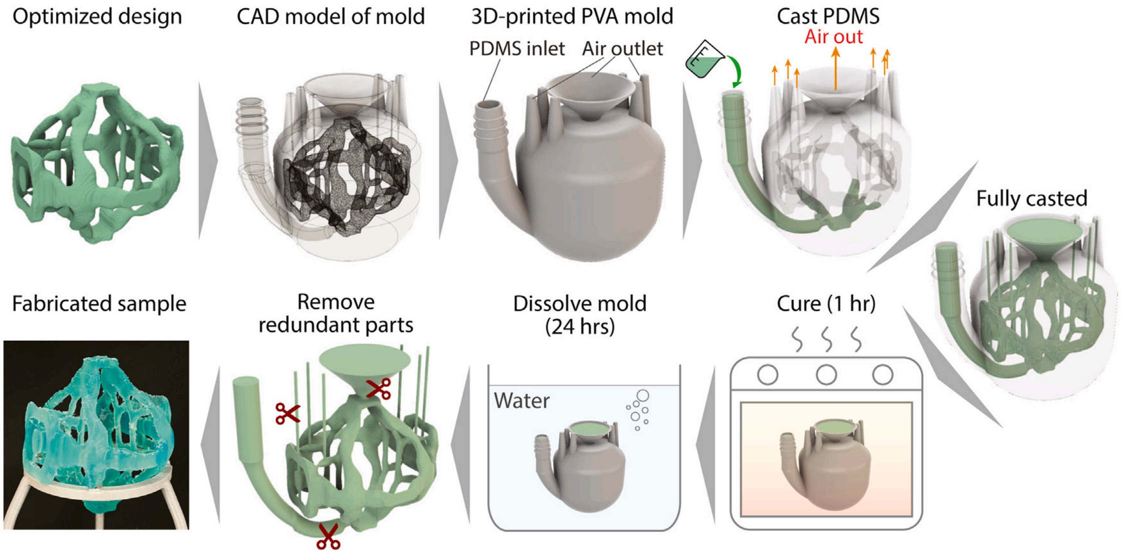

Fig. 8. Proposed hybrid fabrication method tailored for 3D programmed structures combining 3D printed PVA mold and 3D casting of PDMS.

The above analysis reveals unique kinematic features of the overall mechanism: it is heterogeneous in space and asynchronous in time (under quasi-static loading). Dissimilar mechanisms produce the behaviors in the two principal directions, and in the X direction ($H^{(1)}$), the mechanism consists of two sequential sub-mechanisms. While distinct, the three sub-mechanisms operate within one continuum structure and produce highly coupled 3D deformations.

6. Hybrid fabrication of organic 3D design and experimental validation of direction-dependent sequential expansion–contraction behaviors

In this section, we demonstrate physical and precise realization of organic 3D optimized design and its directional sequential expansion–contraction behavior by proposing 3D hybrid fabrication and experiment approaches. We fabricate the programmed structure in Fig. 7 using PDMS (Dow Sylgard 184) with a 20:1 base-agent ratio and green dye (see Appendix B for fabrication process of PDMS). PDMS is suitable for the programmed structures for its large deformation capacity (strains larger than 150%), low viscosity, and ease of fabrication. The main challenge for the fabrication lies in the structure's complex three-dimensional geometries with many details.

To address the above challenge, we propose a hybrid fabrication method (Fig. 8), which is tailored for complex 3D geometries, that combine 3D printing and 3D casting. As shown in Fig. 8, we 3D print the mold of the optimized structure using Fused Deposition Modeling (FDM) printers (Prusa MK3S) with water-soluble Polyvinyl Alcohol (PVA) filaments (MH Build Series PVA). The liquid PDMS is cast into the mold though the inlet tube that connects to the internal slots at the bottom of the mold. Note that, in addition to the internal slots of the structure, the mold has several special components to prevent trapped bubbles during casting. The small air outlet tubes are designed to release air that would otherwise be trapped in dome-like spaces by the rising liquid PDMS upon casting. The funnel at the top is designed to contain extra PDMS when the casting is finished to compensate for potential internal leaks of PDMS. After casting, the PDMS (and the mold) is cured in the oven at 80 °C for 1 h to solidify. Then, the mold is submerged into water for 24 h to dissolve, after which the redundant parts of the specimen are removed. As shown in Fig. 8, the fabricated sample accurately preserves the optimized complex 3D geometries. We note that the proposed hybrid fabrication approach is suitable for 3D structures made with one material. The development of multimaterial fabrication approach for complex 3D geometries is important and planned for future research work.

To load the structure in a universal loading machine, we glue (Loctite® Super Glue Liquid Professional) two 3D-printed, Polylactic Acid (PLA) loading handles to the top and bottom of the fabricated structure as shown in Fig. 9A. The surface of the PLA handle is manually roughened with a utility knife for stronger adhesion. These handles are gripped by the loading machine. As the PLA handles are much stiffer than and firmly glued to the PDMS specimen, they accurately represent the boundary conditions (fixed in the horizontal plane) used in the optimization and FE simulation. The structure is tested using an Instron 68TM-30 universal loading machine with a 500 N load cell and a 5 mm/min overhead speed. As the bottom grip is fixed, the vertical displacement of the machine should be set to twice of those in the designs, i.e., 32 mm. To record the deformation history, we use three cameras to film from top and two horizontal directions, respectively. The lateral deformation i.e., $H^{(1)}$ and $H^{(2)}$, are measured via image tracking based on the footage of the top camera. The details of the proposed experimental setup and image tracking are included in Appendix C and Fig. 9.

The experimental $H^{(1)} - D$ and $H^{(1)} - D$ relations are shown in Fig. 9B with corresponding FE simulation results, and the configurations of the tested specimen at three loading stages are shown in Fig. 9C. The experimental result accurately reproduces

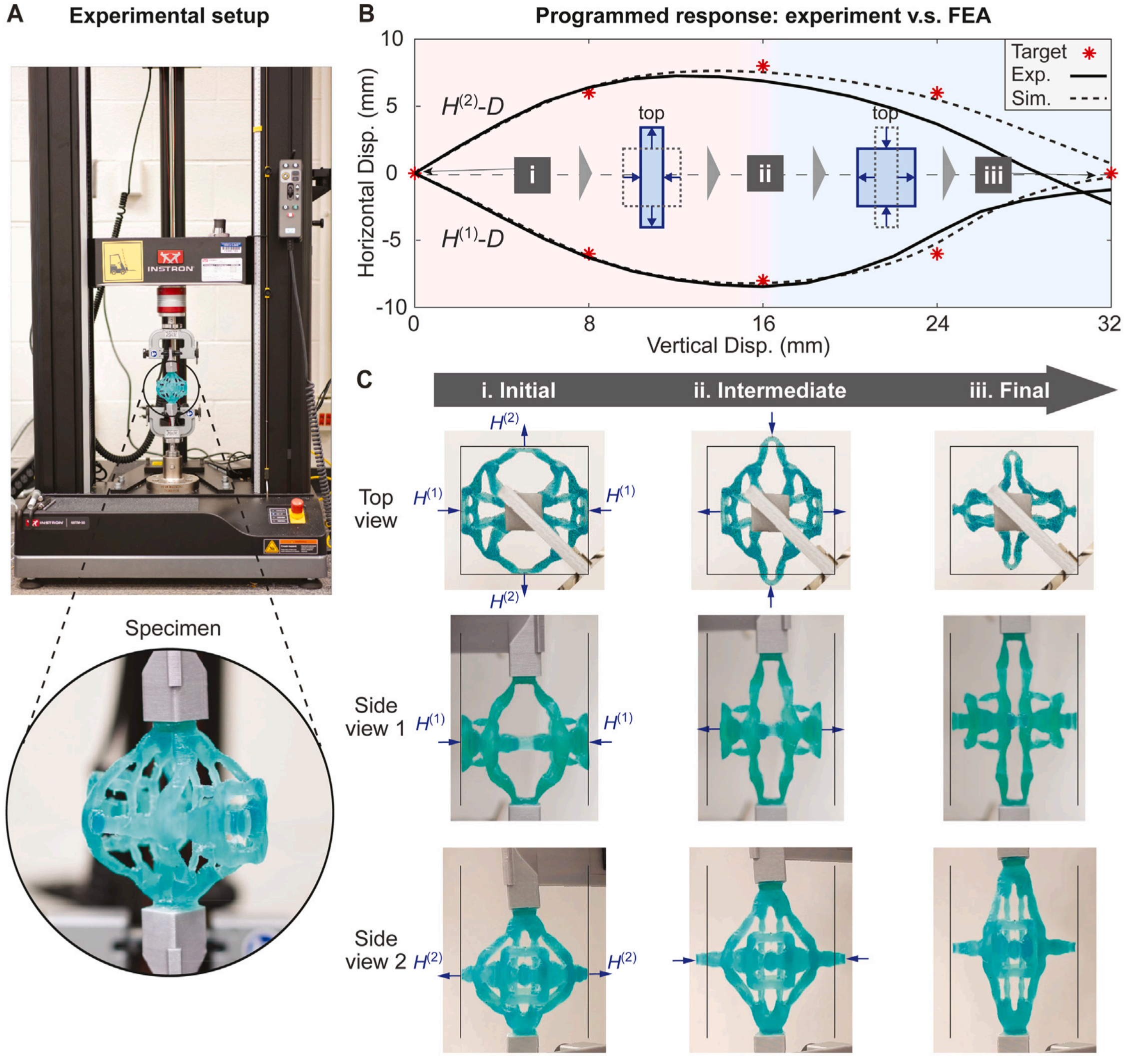

Fig. 9. Experimental validation of programmed metastructure with 3D multi-phase and heterogeneous mechanisms (direction-dependent sequential expansion–contraction) under monotonic loading. (A) Experimental setup; (B) target, experimental, and numerical $H^{(1)} - D$ and $H^{(2)} - D$ responses; (C) experimental configurations of the specimen at initial, intermediate, and final stages.

the sequential contraction–expansion of $H^{(1)}$ and sequential expansion–contraction of $H^{(2)}$ in the non-monotonicity and magnitudes of lateral displacements. The difference between experimental and simulation results are relatively small and appear mostly at the later stage of $H^{(2)}$, where the specimen exhibits greater contracted displacement than the simulation. This may be the result of the slightly asymmetric deformation near the final stage of the specimen, as shown in the corresponding top view in Fig. 9C. The mild asymmetry may be caused by imperfections of fabrication and/or boundary conditions. In addition to programmed response, the deformation patterns and underlying mechanisms are accurately reproduced, as shown in Fig. 9C. In the top views, the experimental configurations show identical patterns as the FE simulation in Fig. 7. Supplementary Video S1 shows the deformation history of the experimentally tested specimen and simulation. The experimental result demonstrates that, although with complex geometry, large deformations, and sophisticated mechanisms, the 3D programmed multi-phase and heterogeneous behaviors are physically and precisely realized.

7. Concluding remarks

Based on multimaterial topology optimization, this study comprehensively explores 3D mechanism space and composite metastructures with unique programmed 3D kinematics/responses (that are not achievable in 2D) under finite deformations. The synthesized structures possess complex 3D geometries and material distributions and accurately achieve a wide range of unconventional deformation patterns under monotonic loading, including counter rotation, direction-dependent expansion and contraction, uniform sequential expansion–contraction, and directional and sequential expansion–contraction. Distinct responses are driven by fundamentally different 3D mechanisms that intelligently exploit material nonlinearity, heterogeneity, large disparity of material properties, optimized geometry, and large deformations and rotations. Some discovered mechanisms are heterogeneous in space and asynchronous in time (under quasi-static loading), consisting of multiple dissimilar yet switchable sub-mechanisms.

A hybrid fabrication method tailored for organic 3D geometries is proposed, which combines 3D printing of PVA mold and 3D casting of PDMS. The 3D optimized design with highly complex geometries is accurately fabricated, and the design's multi-phase and heterogeneous mechanisms are experimentally validated. The experimentally measured response shows high agreement with the target and numerically programmed responses, demonstrating the physical realization of extreme programmed mechanical behaviors. These discovered 3D designs and underlying mechanisms, tailored 3D fabrication approach, and experimental procedures could provide meaningful guidelines for programming function-oriented mechanical metastructures/metamaterials that fully exploit 3D space.

For future work, an extension of the framework to the design of effective nonlinear behaviors and properties of metamaterials could be fruitful. In that context, one can adopt a representative volume method and optimize a unit cell with periodic boundary conditions. Effective properties such as stress–strain relations can be taken as volume-averaged quantities. Alternatively, one can investigate in the direction of nonlinear numerical homogenization, which could offer a more comprehensive description of the effective behaviors for non-orthotropic material structures.

Declaration of competing interest

The authors declare that they have no known competing financial interests or personal relationships that could have appeared to influence the work reported in this paper.

Data availability

Data will be made available on request.

Appendix

The appendices introduce design parameterization of multimaterial topology optimization, interpolation scheme for stored energy density functions, fabrication and characterization of PDMS elastomer, and experimental setup for testing the fabricated programmed structure.

Appendix A. Design characterization of multimaterial structures

This section introduces the filter and projection techniques that map the density and material design variables $\boldsymbol{\rho}$ and $\boldsymbol{\xi}$ to two corresponding physical variables $\bar{\boldsymbol{\rho}}$ and $\bar{\boldsymbol{\xi}}$ used to represent the designs. As both techniques apply in the same format to the two variables, and for conciseness, we use $\boldsymbol{y}$ to represent $\boldsymbol{\rho}$ and $\boldsymbol{\xi}$, and $\bar{\boldsymbol{y}}$ to represent $\bar{\boldsymbol{\rho}}$ and $\bar{\boldsymbol{\xi}}$. The formula for projection is:

$$\bar{y}_e = \frac{\tanh\left(\beta_y \eta_y\right) + \tanh\left(\beta_y\left(\tilde{y}_e - \eta_y\right)\right)}{\tanh\left(\beta_y \eta_y\right) + \tanh\left(\beta_y\left(1 - \eta_y\right)\right)} \tag{A.1}$$

where parameters β_y (representing β_ρ and β_ξ) is a coefficient controlling the discreteness level, parameters $\eta_y = 0.5$ (representing η_ρ and η_ξ) is the projection threshold, and $\tilde{y}_e$ is a corresponding filtered variable of element e computed by

$$\tilde{y}_e = \frac{\sum_{j \in Ne\left(R_y\right)} w_j v_j y_j}{\sum_{j \in Ne\left(R_y\right)} w_j v_j} \tag{A.2}$$

where parameter v_j is the element volume and parameter $w_j = (R - \|\boldsymbol{X}_j - \boldsymbol{X}_e\|_2)^3$ is the weighting factor computed within the set $N_e = \left\{ j \,|\, \|\boldsymbol{X}_j - \boldsymbol{X}_e\|_2 \le R \right\}$. Parameters R_y (representing R_ρ and R_ξ) is the filter radius.

Appendix B. Fabrication and material behavior of dyed PDMS

We use Dow Sylgard 184 and Silc Pig Green to fabricate the dyed PDMS. The base-agent ratio is 20:1, and the weight ratio (weight of the dye to weight of PDMS mixture) of the dye is 0.15%. The base, agent, and dye are mixed together in a tray for 20 min. The mixture is then degassed under −0.8 atmosphere for 1 h, after which the PDMS mixture is cast into the mold of optimized structure.

This study adopts the LP model to describe the behavior of PDMS, with the material constants obtained by least-square fit of uniaxial stress–stretch data. We use the data from one of our previous studies (Li et al., 2022) where the PDMS is fabricated through a procedure identical to this study's. Fig. B1 shows the experimental data and fitted curve of uniaxial stress–stretch relation.

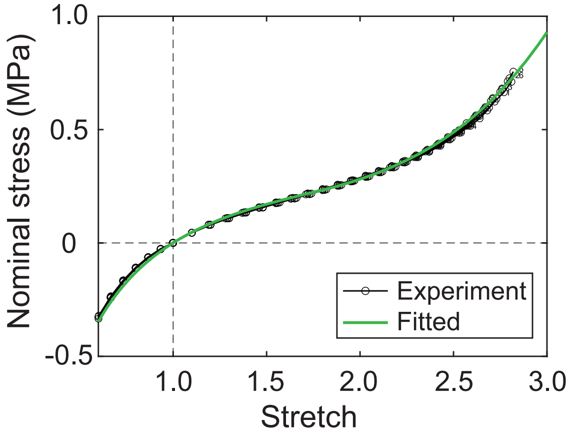

Fig. B1. Uniaxial stress–stretch relation of PDMS.

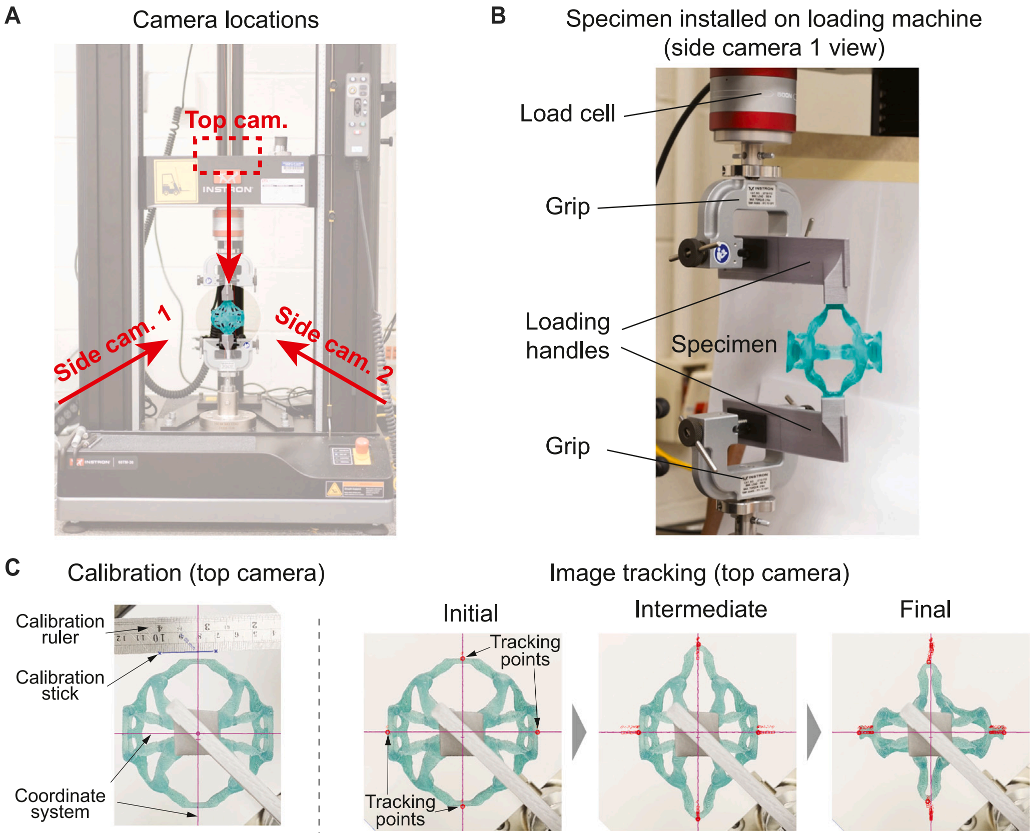

Fig. C1. Experimental setup. (A) Locations of three cameras; (B) specimen installed to the loading machine; (C) calibration and image tracking.

Appendix C. Measuring deformation in experiment

This section provides the details about the experimental setup and image tracking used to measure the structure's lateral displacement. As shown in Fig. C1A, we use three cameras to film the deformation process from three different angles that correspond to the three principal axes of the structure, respectively. For image tracking, we use the footage from the top perspective filmed by a camera mounted to the loading beam of the machine. We use two 3D-printed PLA cantilever-like loading handles to ensure that the specimen would not be blocked by the loading beam when filmed from the top, as shown in Fig. C1B. One ends of the handles are gripped by the machine, and the other ends are glued to the top and bottom of the specimen using superglue. The strong adhesion to the stiff loading handles resembles the boundary condition (fixed in horizontal plane) used in the optimization. Further, the structure is positioned with its principal axes at 45 degrees to the handles so that all four control points can be captured by the top camera. The loading handle would block the view of one control point had the structure's principal axes been aligned with the handle. After initial installation, we adjust the handles to be oriented horizontally using levels.

For image tracking, we mark the structure's control points with black dots. Also, we place a calibration ruler near the structure to be filmed by the top camera for calibration before loading, as shown in Fig. C1C. We use the Tracker software to track the position history of the four control points, as indicated in Fig. C1C. The values of $H^{(1)}$ and $H^{(2)}$ in Fig. 9 are averaged displacements of the two control points in X and Y directions, respectively.

Appendix D. Supplementary data

Supplementary material related to this article can be found online at https://doi.org/10.1016/j.ijengsci.2023.103881.

References

Amir, O., Aage, N., & Lazarov, B. S. (2014). On multigrid-CG for efficient topology optimization. *Structural and Multidisciplinary Optimization*, *49*(5), 815–829. http://dx.doi.org/10.1007/s00158-013-1015-5.

Barrett, R. F., Berry, M. W., Chan, T. F., Demmel, J., Donato, J. M., Dongarra, J. J., et al. (1994). *Other titles in applied mathematics*, *Templates for the solution of linear systems: building blocks for iterative methods*. SIAM, http://dx.doi.org/10.1137/1.9781611971538.

Bendsøe, M. P., & Kikuchi, N. (1988). Generating optimal topologies in structural design using a homogenization method. *Computer Methods in Applied Mechanics and Engineering*, *71*(2), 197–224. http://dx.doi.org/10.1016/0045-7825(88)90086-2.

Bendsøe, M. P., & Sigmund, O. (2003). *Topology optimization: theory, methods and applications*. Springer, Berlin, Heidelberg, http://dx.doi.org/10.1007/978-3-662-05086-6.

Bruns, T., & Sigmund, O. (2004). Toward the topology design of mechanisms that exhibit snap-through behavior. *Computer Methods in Applied Mechanics and Engineering*, *193*(36), 3973–4000. http://dx.doi.org/10.1016/j.cma.2004.02.017.

Chen, Y., Nassar, H., & Huang, G. (2021). Discrete transformation elasticity: An approach to design lattice-based polar metamaterials. *International Journal of Engineering Science*, *168*, Article 103562. http://dx.doi.org/10.1016/j.ijengsci.2021.103562, URL https://www.sciencedirect.com/science/article/pii/S0020722521001063.

Chen, H., Zhu, F., Jang, K.-I., Feng, X., Rogers, J. A., Zhang, Y., et al. (2018). The equivalent medium of cellular substrate under large stretching, with applications to stretchable electronics. *Journal of the Mechanics and Physics of Solids*, *120*, 199–207. http://dx.doi.org/10.1016/j.jmps.2017.11.002, Special issue in honor of Ares J. Rosakis on the occasion of his 60th birthday. URL https://www.sciencedirect.com/science/article/pii/S0022509617307664.

Cheng, G., & Guo, X. (1997). ϵ-Relaxed approach in structural topology optimization. *Structural Optimization*, *13*(4), 258–266. http://dx.doi.org/10.1007/BF01197454.

Cheng, G., & Jiang, Z. (1992). Study on topology optimization with stress constraints. *Engineering Optimization*, *20*(2), 129–148. http://dx.doi.org/10.1080/03052159208941276.

da Silva, G. A., Beck, A. T., & Sigmund, O. (2020). Topology optimization of compliant mechanisms considering stress constraints, manufacturing uncertainty and geometric nonlinearity. *Computer Methods in Applied Mechanics and Engineering*, *365*, Article 112972. http://dx.doi.org/10.1016/j.cma.2020.112972.

Farzaneh, A., Pawar, N., Portela, C. M., & Hopkins, J. B. (2022). Sequential metamaterials with alternating Poisson's ratios. *Nature Communications*, *13*(1), 1041. http://dx.doi.org/10.1038/s41467-022-28696-9.

Feng, Z.-Q., Peyraut, F., & He, Q.-C. (2006). Finite deformations of ogden's materials under impact loading. *International Journal of Non-Linear Mechanics*, *41*(4), 575–585. http://dx.doi.org/10.1016/j.ijnonlinmec.2006.02.003.

Frenzel, T., Findeisen, C., Kadic, M., Gumbsch, P., & Wegener, M. (2016). Tailored buckling microlattices as reusable light-weight shock absorbers. *Advanced Materials*, *28*(28), 5865–5870. http://dx.doi.org/10.1002/adma.201600610.

Fu, K., Zhao, Z., & Jin, L. (2019). Programmable granular metamaterials for reusable energy absorption. *Advanced Functional Materials*, *29*(32), Article 1901258. http://dx.doi.org/10.1002/adfm.201901258.

Goswami, D., Zhang, Y., Liu, S., Abdalla, O. A., Zavattieri, P. D., & Martinez, R. V. (2020). Mechanical metamaterials with programmable compression-twist coupling. *Smart Materials and Structures*, *30*(1), Article 015005. http://dx.doi.org/10.1088/1361-665x/abc182.

Jiao, P., & Alavi, A. H. (2018). Buckling analysis of graphene-reinforced mechanical metamaterial beams with periodic webbing patterns. *International Journal of Engineering Science*, *131*, 1–18. http://dx.doi.org/10.1016/j.ijengsci.2018.06.005, URL https://www.sciencedirect.com/science/article/pii/S0020722518311510.

Kundu, R. D., Li, W., & Zhang, X. S. (2022). Multimaterial stress-constrained topology optimization with multiple distinct yield criteria. *Extreme Mechanics Letters*, *54*, Article 101716. http://dx.doi.org/10.1016/j.eml.2022.101716, URL https://www.sciencedirect.com/science/article/pii/S2352431622000657.

Lee, J., Detroux, T., & Kerschen, G. (2020). Enforcing a force–displacement curve of a nonlinear structure using topology optimization with slope constraints. *Applied Sciences*, *10*, 2676. http://dx.doi.org/10.3390/app10082676.

Li, W., Wang, F., Sigmund, O., & Zhang, X. S. (2021). Design of composite structures with programmable elastic responses under finite deformations. *Journal of the Mechanics and Physics of Solids*, *151*, Article 104356. http://dx.doi.org/10.1016/j.jmps.2021.104356, URL https://www.sciencedirect.com/science/article/pii/S0022509621000533.

Li, W., Wang, F., Sigmund, O., & Zhang, X. S. (2022). Digital synthesis of free-form multimaterial structures for realization of arbitrary programmed mechanical responses. *Proceedings of the National Academy of Sciences*, *119*(10), Article e2120563119. http://dx.doi.org/10.1073/pnas.2120563119, arXiv:https://www.pnas.org/doi/pdf/10.1073/pnas.2120563119. URL https://www.pnas.org/doi/abs/10.1073/pnas.2120563119.

Li, M., Zhu, K., Qi, G., Kang, Z., & Luo, Y. (2021). Wrinkled and wrinkle-free membranes. *International Journal of Engineering Science*, *167*, Article 103526. http://dx.doi.org/10.1016/j.ijengsci.2021.103526, URL https://www.sciencedirect.com/science/article/pii/S0020722521000732.

Lopez-Pamies, O. (2010). A new I1-based hyperelastic model for rubber elastic materials. *Comptes Rendus Mécanique*, *338*(1), 3–11. http://dx.doi.org/10.1016/j.crme.2009.12.007, URL https://www.sciencedirect.com/science/article/pii/S1631072109002113.

MATLAB (2020). *version 9.9.0 (R2020b)*. Natick, Massachusetts: The MathWorks Inc..

Ogden, R. W. (1997). *Non-linear elastic deformation*. Dover Publications.

Olhoff, N. (1989). Multicriterion structural optimization via bound formulation and mathematical programming. *Structural Optimization*, *1*(1), 11–17. http://dx.doi.org/10.1007/BF01743805.

Restrepo, D., Mankame, N. D., & Zavattieri, P. D. (2015). Phase transforming cellular materials. *Extreme Mechanics Letters*, *4*, 52–60. http://dx.doi.org/10.1016/j.eml.2015.08.001, URL https://www.sciencedirect.com/science/article/pii/S2352431615000929.

Saad, Y., & Schultz, M. H. (1986). GMRES: A generalized minimal residual algorithm for solving nonsymmetric linear systems. *SIAM Journal on Scientific and Statistical Computing*, *7*(3), 856–869. http://dx.doi.org/10.1137/0907058, arXiv:https://doi.org/10.1137/0907058.

Sigmund, O. (1994). Materials with prescribed constitutive parameters: An inverse homogenization problem. *International Journal of Solids and Structures*, *31*(17), 2313–2329. http://dx.doi.org/10.1016/0020-7683(94)90154-6.

Sigmund, O. (1995). Tailoring materials with prescribed elastic properties. *Mechanics of Materials*, *20*(4), 351–368. http://dx.doi.org/10.1016/0167-6636(94)00069-7.

Sigmund, O. (2001). Design of multiphysics actuators using topology optimization – part II: Two-material structures. *Computer Methods in Applied Mechanics and Engineering*, *190*(49), 6605–6627. http://dx.doi.org/10.1016/S0045-7825(01)00252-3.

Svanberg, K. (1987). The method of moving asymptotes—a new method for structural optimization. *International Journal for Numerical Methods in Engineering*, *24*(2), 359–373. http://dx.doi.org/10.1002/nme.1620240207.

Wang, F. (2018). Systematic design of 3D auxetic lattice materials with programmable Poisson's ratio for finite strains. *Journal of the Mechanics and Physics of Solids*, *114*, 303–318. http://dx.doi.org/10.1016/j.jmps.2018.01.013.

Wang, F., Lazarov, B. S., & Sigmund, O. (2011). On projection methods, convergence and robust formulations in topology optimization. *Structural and Multidisciplinary Optimization*, *43*(6), 767–784. http://dx.doi.org/10.1007/s00158-010-0602-y.

Wang, F., Lazarov, B. S., Sigmund, O., & Jensen, J. S. (2014). Interpolation scheme for fictitious domain techniques and topology optimization of finite strain elastic problems. *Computer Methods in Applied Mechanics and Engineering*, *276*, 453–472. http://dx.doi.org/10.1016/j.cma.2014.03.021.

Wang, F., & Sigmund, O. (2021). 3D architected isotropic materials with tunable stiffness and buckling strength. *Journal of the Mechanics and Physics of Solids*, *152*, Article 104415. http://dx.doi.org/10.1016/j.jmps.2021.104415, URL https://www.sciencedirect.com/science/article/pii/S002250962100096X.

Wang, F., Sigmund, O., & Jensen, J. (2014). Design of materials with prescribed nonlinear properties. *Journal of the Mechanics and Physics of Solids*, *69*, 156–174. http://dx.doi.org/10.1016/j.jmps.2014.05.003.

Wang, C., Zhao, Z., Zhou, M., Sigmund, O., & Zhang, X. S. (2021). A comprehensive review of educational articles on structural and multidisciplinary optimization. *Structural and Multidisciplinary Optimization*, *64*(5), 2827–2880. http://dx.doi.org/10.1007/s00158-021-03050-7.

Xue, Z., Song, H., Rogers, J. A., Zhang, Y., & Huang, Y. (2020). Mechanically-guided structural designs in stretchable inorganic electronics. *Advanced Materials*, *32*(15), Article 1902254. http://dx.doi.org/10.1002/adma.201902254, URL https://onlinelibrary.wiley.com/doi/abs/10.1002/adma.201902254. arXiv:https://onlinelibrary.wiley.com/doi/pdf/10.1002/adma.201902254.

Yang, Y., Fu, C., & Xu, F. (2020). A finite strain model predicts oblique wrinkles in stretched anisotropic films. *International Journal of Engineering Science*, *155*, Article 103354. http://dx.doi.org/10.1016/j.ijengsci.2020.103354, URL https://www.sciencedirect.com/science/article/pii/S0020722520301415.

Zhang, X. S., Chi, H., & Paulino, G. H. (2020). Adaptive multi-material topology optimization with hyperelastic materials under large deformations: A virtual element approach. *Computer Methods in Applied Mechanics and Engineering*, *370*, Article 112976. http://dx.doi.org/10.1016/j.cma.2020.112976.

Zhang, Y., Velay-Lizancos, M., Restrepo, D., Mankame, N. D., & Zavattieri, P. D. (2021). Architected material analogs for shape memory alloys. *Matter*, *4*(6), 1990–2012. http://dx.doi.org/10.1016/j.matt.2021.04.015, URL https://www.sciencedirect.com/science/article/pii/S2590238521001764.

Zhang, H., Wang, Y., & Kang, Z. (2019). Topology optimization for concurrent design of layer-wise graded lattice materials and structures. *International Journal of Engineering Science*, *138*, 26–49. http://dx.doi.org/10.1016/j.ijengsci.2019.01.006, URL https://www.sciencedirect.com/science/article/pii/S0020722518323450.